Ionospheric and stratospheric electric field responses to an extreme solar energetic particle event

Edgar A. Bering, III[1], Michael Kokorowski[2], John G. Sample[3], Robert H. Holzworth[4], Michael P. McCarthy[4], Robyn M. Millan[5], Leslie Woodger[5], David M Smith[6], Juan V. Rodriguez[7]

Corresponding Author: Edgar A. Bering, III, Physics and ECE Departments, 3507 Cullen Blvd., #617, University of Houston, Houston, Texas, 77204-5005, USA, *eabering@uh.edu*

Key Points

- High latitude global circuit was effectively shorted out by a solar energetic particle event.
- Ionospheric convection was very weak for several hours following the event.
- Stratospheric electric field was briefly reversed by magnetospheric forcing.

Abstract. This paper will report on the effects of an extreme space weather event. On January 20th, 2005, a balloon-borne experiment intended to measure relativistic electron precipitation and its effects was aloft over Antarctica (~32 km; near 70º S, 345º W geographic) throughout the duration of the solar energetic particle (SEP) event. The balloon carried an x-ray scintillation counter, dc electric field, and scalar electrical conductivity sensors. Intense energetic proton precipitation and large increases in the energetic proton population of the outer radiation belts were observed by a global array of observatories and spacecraft. The stratospheric conductivity increased by nearly a factor of 20 above ambient at the time of the SEP event onset and returned to within a factor of two above normal levels within 17 hours. The electric field decreased to near zero following the increase in particle flux at SEP onset. Combined with an atmospheric electric field mapping model, these data are consistent with a shorting out of the global electric circuit and point toward substantial ionospheric convection modifications. It is shown that the conductivity profile predicted by the Sodankylä Ion and Neutral Chemistry (SIC) model does not shield the balloon payload at 32 km

[1] Physics and ECE Departments, University of Houston, Houston, Texas, USA
[2] Jet Propulsion Laboratory, Pasadena, California, USA
[3] Space Sciences Laboratory, University of California at Berkeley, Berkeley, California, USA
[4] Department of Earth and Space Science, University of Washington, Seattle, Washington, USA
[5] Dartmouth College, Dept. of Physics and Astronomy, Hanover, New Hampshire, USA
[6] University of California at Santa Cruz, SCIPP, Santa Cruz, California, USA
[7] Ball Aerospace, Boulder, Colorado, USA; Formerly at University of Colorado, CIRES, Boulder, Colorado, USA

from the ionospheric horizontal field. Thus, the data really do indicate a very low level of ionospheric convection over the balloon during the 6 hours following the SEP event. We have used global magnetometer and satellite data to interpret the changes in the vertical field as indicators of large scale convection changes.

Plain Language Summary

This paper reports the way a major solar flare drove changes in the electrical connection between the outer reaches of the Earth's atmosphere (the magnetosphere) and the stratosphere. These effects were observed by a stratospheric balloon payload over the Waddell Sea near Antarctica on January 25, 2005. Three major effects were seen and discussed. The Earth's global circuit shorted out. Second, the ionospheric electric field went to zero. Third, the initial recovery of the global circuit was initially driven by magnetospheric signals.

1. Introduction

The Earth's global electric circuit has been studied extensively for more than a century [*Israel*, 1973; *Reiter*, 1992; *Roble and Tzur*, 1986]. In broad terms, the circuit consists of two conductors, the Earth itself and the ionosphere, separated by a resistive medium, the lower atmosphere [*Bering et al.*,1998; *Ibid.*,]. The circuit has three drivers, thunderstorm activity in the troposphere, an ionospheric dynamo driven by solar diurnal tides, and the convection potential imposed on the ionosphere by the interaction of the solar wind with the magnetosphere. While each of these sources has been well studied, the coupling between these three current systems remains poorly understood, particularly during intervals of extreme space weather. The purpose of this paper is to continue a study of the response of the global circuit to one of the most extreme space weather events of the spacecraft era, the solar energetic proton (SEP) event of 20 January 2005. This SEP event was the hardest and most intense event observed since 1956 [*Mewaldt et al.*, 2005].

Fortuitously, the SEP event occurred during the second Antarctic flight of the 2005 MINIature Spectrometer (MINIS) balloon campaign. The main scientific objective of the MINIS campaign was to study relativistic electron precipitation events in the plasmapause region. Each balloon payload carried a large crystal X-ray scintillation counter, a 3-axis quasi-static electric field detector, and a VLF receiver [*Kokorowski et al.*, 2008; *Kokorowski et al.*, 2006; *Millan et al.*, 2005, 2008, 2012]. The electric field detector also made stratospheric conductivity measurements every 10 minutes. Data from these detectors have been previously reported [*Ibid*]. The data contained previously undiscussed features that resisted initial efforts at interpretation. The major questions are: Does the observed small value of the horizontal electric field, E_{hor}, really represent magnetospheric conditions? What happens to the magnetosphere when the ionospheric conductivity becomes very large? How do we understand the abrupt jumps and change in sign in the vertical electric field, E_{vert}?

This paper will attempt to address these questions. In the next section, we review the overall solar and geophysical background of the event. The third section will give a brief discussion of the MINIS instrumentation, followed by a summary of the relevant observations. The discussion section will engage with the questions followed by summary and conclusions.

2. January 2005: An Overview

2.1. Sun and Solar Wind

The third week of January in 2005 was an unusually active interval on the Sun (Figure 1). Starting on 15 January, the solar X-ray detector on GOES 12 observed 4 X and one M8.6 class flares, as shown in the top panel of Figure 1. The last of these was an X7.1/2b proton flare at 06:36 UTC on 20 January 2005. This flare produced an intense solar energetic proton (SEP) event. This event was the hardest and most energetic proton event of Cycle 23. The SEP had a hard enough spectrum to penetrate the entire atmosphere at latitudes as low as Athens, Greece. The bottom panel of Figure 1 shows hourly averages of the McMurdo neutron-monitor counting rate that responded very strongly to the solar ground level event. The GOES proton panel shows that the >10 MeV protons peaked at 0810 UTC and returned to background at 1755 UTC on 22 January.

There were four major coronal mass ejections (CMEs) during this interval: a halo CME at 22:25 on 15 January with V_{sw} = 1850 km/s, a fast CME at 07:02 on 17 January with V_{sw} = 2400 km/s, a halo CME 08:03 on 19 January with V_{sw} = 1960 km/s, and a halo CME at 06:36 on 20 January.

The interplanetary magnetic field (IMF) and solar wind conditions that prevailed near the Earth during the week of 16-22 January 2005 are shown in Figures 2 and 3. From bottom to top, the panels of Figure 2 show 64-s averages of the GSM *x*-, *y*-, and *z*-components and total field magnitude of the IMF observed by the ACE spacecraft in the upstream solar wind. In the same order, Figure 3 shows 64-s averages of the density, temperature, and flow velocity of the solar wind also observed by SWEPAM on ACE. In this paper, we focus on the 12-hour interval starting with the X7.1 flare.

The data in Figure 2 show that the shock wave from the 15 January CME arrived at ACE at 10:42 UTC on 17 January. The IMF was disturbed and/or elevated for the next ~2 days. The arrival time of the CME from 17 January was obscured by the on-going activity. The IMF quieted and the field magnitude relaxed to quiet time levels starting at ~1000 UT on 19 January. The IMF was in a quiet state by 0000 UTC on 20 January. The IMF turned northward at ~1500 on 18 January, There was an interval weakly southward field from 1000 to 1300 UTC on 19 January. The field turned strongly northward at ACE at 2000 UT on the 19th, relaxing to B_z*~0* at 1300 UT on the 20th.

Figure 3 shows the properties of the solar wind during this week. The data gaps are the result of intervals of high energetic background contamination from the two large SEP events during this period. The data indicate that the Earth encountered a hot, low-density high-speed stream at 10:42 UTC on 17 January. The end of the high-speed stream was gradual rather than discontinuous. The solar wind speed started slowing early on the 19th and continued to recover until the arrival of the next big CME on 21 January. The temperature increased by an order of magnitude in the first stream, but cooled relatively quickly to more normal solar wind levels early on the 19th. A hot region was encountered at about midnight UT on the 20th.

The IMF data from ACE (Figure 4) indicate that the E-field steps discussed in this paper occurred during a period of weakly southward IMF. The IMF turned abruptly southward at 1318 UT and remained so for several hours. There was no large change in the IMF components until c. 1730 UT, after the second E-field step. The ACE SWICS proton data in Figure 5 indicate that the solar wind velocity was rather high and decreasing slowly during this period from ~800 km/s at 1200 to ~700 km/s at 1800 UT. There was a rapid increase in dynamic pressure around the time of the IMF southward turning when the proton density increased from 0.28 (at 1305) to 2.9 cm^{-3} (at 1330). The southward turning and associated pressure increase may have led to the first injection. (These times are not delayed for propagation time from L1 to the magnetopause; at the observed solar wind speeds, the delay is about 0.5 hr.)

2.2. Geospace

2.2.1. Ring Current. The D_{st} magnetic index for a two week interval including 20 January is shown in the lower panel of Figure 6. The D_{st} index is proportional to the energy content of the

ring current. The data shown in Figure 6 confirm our expectation based on the solar flare data. There was a -90 nT geomagnetic storm on 18 January. Recovery and ring current decay had reduced the level of disturbance to ~-50 nT by 20 January.

2.2.2. Auroral Electrojet. The top panel in Figure 6 is a plot of the K_p geomagnetic index for the same two week interval. K_p is a logarithmic measure worldwide geomagnetic disturbance. As such, it responds to a combination of auroral electrojet, ionospheric convection, and geomagnetic micropulsation activity. K_p for the six hours before the flare was low, ~2, but not zero. K_p rose to around 4 at 1200 UT, largely owing to wave rather than electrojet activity, as indicated in Figure 7, which plots the auroral electrojet index AE for 20 January, 2005.

As expected, the electrojets were very active for most of 19 January (not shown) but were diminishing strongly by 0000 UT on 20 January. The six hours leading up to the flare were characterized by AE near zero, indicating an absence of convection or electrojet activity. This situation persisted, virtually unchanged, for the next six hours. The low AE value between 0600 and 1200 is somewhat inconsistent with the K_p values shown in Figure 6. A possible interpretation will be discussed below.

After many hours of very low AE index levels, there was a small increase in the AE index (<500 nT) just prior to the second electric field step c. 1400 UTC and a larger increase (>1000 nT) around 1545 UTC, prior to the third electric field step c. 1600. The solar wind data, geostationary particle observations, and the AE index together create the picture of a period of magnetospheric convection driven by weakly southward IMF, punctuated twice by particle injections.

3. The MINIature Spectrometer (MINIS) Experiment

The three major instruments on the MINIS balloon payloads discussed here are: an MeV X-Ray scintillation counter [*Kokorowski et al.*, 2006; *Millan*, 2011; *Millan et al.*, 2007], a 3 axis double probe electric field meter [*Holzworth and Bering*, 1996; *Mozer and Serlin*, 1969], and a relaxation conductivity measurement [*Byrne et al.*, 1988]. All three instruments been described at length in previous papers [*Ibid.*]. Briefly, the scintillation counter detected X-rays from 25 keV to 10 MeV. The data from this detector were telemetered in two formats, four broad-band energy channels, sampled every 50 ms, and a 208 channel energy spectrum, integrated over 8 s intervals. The electric field sensor had a maximum dynamic range of 400 mV/m in the horizontal axis and 7 V/m in the vertical axis. The instrument had three axes, and was rotated about the vertical axis with a 44 s period. The data were sampled 1/s in ordinary operation. If one of the horizontal pairs failed, a full vector measurement was still made once per spin. During conductivity measurement cycles, which occurred every 10 min, the data were sampled at 30 Hz for 15 s.

The gains of the electric field channels were calibrated before flight using a precision voltage source. The electronic DC offsets of all three axes were calibrated in flight during the conductivity measurement. Work function and geometric offsets of the horizontal channels were calibrated in flight by least-squares fitting a sinusoid at the rotation period to the raw data. It is not possible to perform an in-flight calibration of the work function offset of the vertical component channel.

The horizontal component of the ionospheric electric field maps to the balloon through the weakly conducting lower atmosphere. This mapping process acts as a temporal low pass filter and a spatial long-wavelength (small k) filter. Under normal circumstances, a balloon at 32 km

will detect the ~1 s, 100 km average of the overlying ionospheric electric field [*Mozer and Serlin*, 1969].

4. The 20 January Solar Flare

4.1 Flare Parameters

There was an X7.1/2b proton flare that began at 06:36 UTC on 20 January, 2005 [*Mewaldt et al.*, 2005; *Kokorowski et al.*, 2006]. The earliest detection of the GLE onset was at 0649 UTC in neutron monitor data and at 0650 UTC in GOES data [*He and Rodriguez*, 2018]. The >100 MeV GOES proton flux reached a peak intensity of 652 proton flux units (PFU) at 0710 UTC. As noted above, the flare produced the hardest, most energetic solar energetic proton (SEP) event of solar cycle 23.

The SEP event was hard enough to produce very substantial increases in neutron monitor counting rates at ground level observatories (Figure 8), and has been designated Ground Level Event (GLE) 69 [*He and Rodriguez*, 2018; *Moraal et al.*, 2005]. The lowest latitude, highest rigidity station that observed the event was a 2% increase at Athens, with a cutoff rigidity of 8.4 GV. Despite its unusual intensity and hardness, the GLE only lasted about a day, which was a shorter than average duration.

4.2 MINIS data

4.2.1 Flare Details. Figure 9 shows the details of the balloon data from payload 2S at the time of the flare event. At this time, the balloon was at ~62° S geomagnetic latitude, ~0450 MLT, and an altitude of ~32 km. From top to bottom, the top three panels show the three components of the electric field in earth-fixed geomagnetic coordinates, vertical, horizontal poleward, and horizontal eastward in units of V/m at a one Hz sample rate. The bottom panel shows an energy-time spectrogram of the X ray data. The vertical axis is photon energy from pulse-height-analyzer channels. The horizontal axis for all four panels is UTC on 20 January 2005.

Figure 9 begins prior to the start of the X-ray flare. Prior to 06:56, the Figure shows normal data for the sub-auroral pre-noon location of the payload. The vertical electric field averaged slightly negative, with a moderate level of variation. The horizontal components had small but non-zero dc averages and showed a moderate amount of fluctuation. The x-ray spectrogram was acquired over 32 s integration periods. It shows several features in different energy ranges. The expected annihilation line was prominent at 511 keV. This line appeared to waver and bend upward near 06:53. Because this line has fixed energy, its variation is an instrumental artifact, possibly arising from a shifting baseline associated with the unusual high-energy fluxes. Two other weak line features became noticeable near 06:45, one at 900 keV and another just above 2 MeV. Although the feature near 900 keV is not understood, the 2.223 MeV line is known to be the neutron capture line on hydrogen at 2.223 MeV at the Sun. This line was also seen at RHESSI at the same time (06:45). RHESSI measured the energy precisely [*Shih et al.* ,2009]. Increased fluxes between 25 and 200 keV near 06:46 were X-radiation from the solar flare. A second, weaker, fluctuation below 150 keV and between 06:52 and 06:56 was also from the flare. Above 1 MeV, there were three increasing flux steps: one at 06:46, when the 2 MeV line feature appeared; a second at 06:52, when the 2 MeV line feature became less noticeable; and a third at 06:56 when fluxes dramatically increased even to 8 MeV energy.

The situation changed abruptly at 06:56 UTC. The total counting rate in the photomultiplier tube increased by orders of magnitude over the entire energy range. This very high counting rate had some unfortunate consequences. First, the phototube-telemetry interface had the highest interrupt priority. At a high interrupt rate, the data processor failed to adhere to its schedule, thereby disrupting the

preparation of data packets and their emission into a telemetry stream. This effect resulted in long gaps between recovered electric field or spectrum measurements. Second, under a barrage of high energy radiation, the photomultiplier draws an unusually high current, which feeds back to disturb its bias voltages, and thereby reduces its gain. This effect is the likely mechanism by which the high energy part of the spectrum disappeared near 06:57.

The abrupt increase in counting rate at 06:56 or so occurred ~ 5 min after the event onset was detected at GOES 11, shown in the third panel in Figure 10. (The GOES plot shows 5 min bins that were time stamped at the start of the 5 min interval.) We interpret this increase as the time of main proton precipitation onset at the balloon location. It was most likely the result of an increase in the proton flux, since 07:01 was the reported time of the maximum in X-ray flux. GOES X-ray flux cannot be compared directly with the MINIS spectrometer, since the GOES X-ray energies are too low to register on MINIS. The flare did produce much higher energy X-rays as seen by HESSI [*Mewaldt et al.,* 2005]. The RHESSI profile agreed very well with MINIS light curve. The X-ray event did not seem to extend above 200 keV at MINIS. The counts above 500 keV were probably produced by energetic protons or electrons. The 2.223 neutron capture line is always the second-brightest solar hard x-ray line, after positron annihilation, produced by flares that accelerate a lot of ions into the solar photosphere [*Shih et al.,* 2009]. Of the flares observed by RHESSI from 2002 t0 2005, this flare was second only to the 2003 Halloween storm flare in 2.223 MeV fluence. The increase in X-ray flux at 06:52 does coincide with proton arrival at GOES. Anything above background at high energy after 06:52 has to have been from energetic particles either directly (particle hits detector) or indirectly (particle causes x-ray/gamma-ray which gets to detector with or without additional reactions).

The effect of the proton event on the electric field is interesting, and the main topic of this paper. What the top three panels indicate is that the dc level of all three components decayed to zero in about 200 s. Each component also showed much lower fluctuation amplitude than before the event. As will be shown below, the field stayed that way for the next several hours.

4.2.2 Flare Aftermath. The real purpose of this paper is to try to explain and understand the behavior of the global electric circuit over the next 12 hours. Figure 10 compares some of the balloon data with energetic proton and magnetic field data observed at geosynchronous orbit by the GOES-11 and -12 spacecraft.

Panel 10(a) at the top of the figure shows 1 min averages of the vertical electric field measured by MINIS Flight 2S for all of 20 January 2005. Prior to the flare, the vertical electric field was ~-0.2 V/m (positive is upward) with a ~50 mV/m variance: a typical fair weather signature. As discussed above, after the flare, the vertical electric field decayed to zero (the first jump) and stayed near zero for ~ 3 hours. At that point, the vertical field began to recover slowly toward the pre-flare value. The most important features in this panel are the second and third sharp upward jumps in the field at ~1400 and ~1600 UT. At these jumps, the vertical field first returned to nearly zero, then turned positive, reaching ~+0.1 V/m. This inversion of the electric during fair weather is a unique observation. We mark the times of the flare and the following two jumps with dashed lines in several of the following figures. The underlying causes of these jumps is one of the two main issues in this paper.

Panel 10(b), second from top, shows the negative ion conductivity measured by the relaxation technique [*Byrne et al.,* 1988]. The measurement was made every ten minutes, alternating between two of the horizontal field probes, 1 and 3. The data from each probe was transmitted on two channels, potential vs payload ground, and potential difference with respect to the opposite probe on the same axis, 2 and 4. The results were four data sources for the negative ion conductivity estimate. Since the probes are also responding to changes in the ambient field, there can be differences between

the estimates. These differences provide an estimate of the uncertainties and systematic errors in the data. Figure 10(b) plots all of the data channels using 4 distinct symbols [*Kokorowski et al.,* 2012] (K12). The panel shows a nearly 20-fold increase of the stratospheric negative ion conductivity near the balloon payload immediately after the flare. This increase prompted a modeling effort aimed at understanding what the SPE event did to the overall conductivity profile of the stratosphere and mesosphere (K12). This paper will apply the results of that modeling to try to understand the other observations.

The key features of importance in panel 10(c) are the increases in the >1MeV proton counting rates seen at the same time as the jumps. It appears that there is reason to interpret the jumps as resulting from large scale magnetospheric processes. Each of the jumps was preceded by a change in the magnetic field at GOES and Southern Hemisphere neutron monitor stations South Pole, McMurdo, and Terre Adelie. At these stations, this rapidly-rising GLE peaked 1-3 minutes before 06:56. However, it was a very anisotropic and multi-peaked event [*Plainaki et al.,* 2007]. This spatial and temporal structure, as well as the different energies dominating the effect at balloon altitude vs. ground level, probably led to the slightly delayed response at the balloon. Panel 10(d) indicates that a dipolarization occurred ~30 m prior to the second jump. The tail field began stretching out again about an hour before the third jump and was barely back to the pre-second-jump configuration when the third jump occurred. These variations seem to indicate that the jumps were associated with changes in the electric currents flowing in the magnetosphere. We will examine these changes in the next section.

Figure 11 shows the horizontal electric field data plotted as equivalent ionospheric convection in clockdial format. The view is down on the South Pole, which makes the clockface correspond to a normal clock. The outer ring gives the magnetic local time, The inner ring shows the UT of the observations, with the UT-MLT conversion fixed at the start of the interval shown. The bar between the rings shows the geomagnetic latitude of the balloon. The base of each one min average data arrow is at the location of the balloon at the indicated UT. The arrow represents the ionospheric flow velocity vector. The top of the figure shows that typical sub-auroral flows were occurring pre-flare. The disappearance of horizontal flow at the time of the flare is very evident. Very little recovery has occurred by the end of the day.

Figure 12 shows all three components of the electric field at the highest available time resolution. The field has been de-spun from payload coordinates and is plotted in local geomagnetic coordinates, co-rotating with the Earth. The data rate was 1 sample/s for the horizontal and 4 sample/s for the vertical components. The second panel from the top shows the raw vertical data, while the top panel shows the vertical field data with the spin rate residual removed. The data dropouts result from a combination of the high count rate in the X-ray detector and lost Iridium calls. There were also brief cutouts every ten minutes that are the result of not plotting data during the conductivity measurements. The first or flare jump is not shown in this Figure. Unfortunately, both the 2nd and 3rd jumps were closely coincident with data dropouts. This proximity appears to have been a coincidence. The jumps take less than a minute and appear to have been associated with sharp negative spikes in the vertical field and noise bursts in the horizontal. The combination of sharp spikes and a data drop out gives the least-squares sine wave detection portion of the despin algorithm severe difficulties, which means that we cannot discuss the details of the spikes with any confidence. All we can say is that there were noise bursts in the 0.1-0.5 Hz range.

4.2.3 Step Perturbation Context This subsection will make the case that the magnetosphere was a likely source of the second and third step perturbations. The first upward step in E_{vert} is clearly a result of the flare. Let us begin by focusing on the timing shown in a 4 hour interval that contains the problematic steps (second and third) as shown in Figure 12. The data had many gaps during this time.

Two of these gaps fell during the actual step transitions. For the second step (first shown), the gap was aligned so that we can see both ends of the transition, at ~13:56:30 and 14:02. The third step (second shown) began at 15:54:40 and ended during the data gap that follows before 16:04.

The first comparison plot is Figure 13, showing the maximum rate data from the P1 (0.6-4 MeV) channels on GOES 10, 11, and 12. These protons are not energetic enough to reach balloon altitude. The flux variations are understood to be simply markers of changes in magnetospheric dynamics. These geosynchronous platforms are at 134.5, 107.5 and 75.2 W longitude respectively. Their NH conjugate footpoints are shown in Figure 14. The GOES position circles are the size of the modelling uncertainty. There were flux increases in the P1 channel at all three gosynchronous spacecraft beginning slightly before the second step at 1400, with a bipolar fluctuation at GOES 10 coincident with the step. The GOES 12 order of magnitude flux increase was largest. The flux increases at the time of the third step are more puzzling. GOES 10 observed an increase of nearly 2 orders of magnitude, starting just before the step. GOES 11 saw an order of magnitude increase beginning during the step, whereas GOES 12 observed a slow, modest enhancement that also began during the step transition.

The flux increases in the channel (0.6-4 MeV) were probably due to energetic proton injections near midnight [*Baker et al.,* 1979]. This conclusion is corroborated by the AE index shown in Figure 7, as discussed above. At 1400 UT, the locations of the GOES satellites spanned dawn to mid-morning local times (10: 5 LT, 11: 7 LT, 12: 9 LT). At 1600, the satellites were two hours closer to noon. Given that protons gradient-curvature drift from east to west (through decreasing local time), by the time the first proton injection (associated with the second E-field step) was observed at the GOES satellites, the protons had drifted through ~15-19 hours of local time. At onset, the second injection (associated with the third step) had drifted through ~13-17 hours of local time. (The drift period of 1 MeV protons at L = 6.6 is ~6 min.) However, the fact that GOES-West (-10) observed the second injection first and GOES-East (-12) observed it last, suggests that the simple picture of east-to-west drift following injection at midnight is not adequate to describe what happened here.

To understand the observations, it is first necessary to recognize that the detectors on GOES-10 and -12 look eastward and westward, respectively, observing proton fluxes with gyrocenters inside and outside GEO, respectively [*Rodriguez et al.,* 2010]. The gyroradius of a 1 MeV proton at geostationary orbit (in a 100-nT magnetic field) is 0.2 Re. GOES-10 observed a smaller injection c. 1400 and a larger injection c. 1600 relative to GOES-12. The fluctuations in the data from the spinning GOES-11 satellite confirm that there was a large flux gradient during both injections, with the flux increasing radially outward (over two gyroradii) during the first and decreasing outward during the second. The observations suggest that the injected “cloud” of protons reached further inside the magnetosphere during the second injection, affecting its transport to the observing satellites.

Figure 15 shows 24-hour plots of all three components of the perturbations in the magnetic field from the observatories on the west coast of Greenland. The 1400 feature appeared as a relatively short pronounced spike in all three components at all stations south of 80° N geomagnetic latitude. The eastward or Y component also showed a short positive spike at the six southern stations at 1600 UT.

The next two figures show 4-hour plots of the X and Y components of the magnetometer data from the stations that are located in Figure 14 for the same time interval as Figures 12 and 13. The ~1400 event was clearly evident in both components at all stations. The ~1600 event was more localized. The east/Y/D spike at 1600 that can be seen in the middle panel of Figure 15 appears in the bottom two panels of Figure 17. It seems the event was extended N-S but confined in longitude. The absence of a spike at STJ reflects the low latitude of that station.

These data are strong evidence that the second and third steps in the electric field data were effectively simultaneous with large-scale changes in current flow and convection in the magnetosphere.

5. Discussion

These data and observations pose three important questions:

- Does the near-zero value of the electric field really represent atmospheric and magnetospheric conditions, or is it a localized ionospheric or instrumental artifact resulting from the high conductivity?
- Conversely, what is the magnetospheric effect of the very high ionospheric conductivity?
- What caused the second and third jumps in the vertical electric field?

In this section, the paper will elaborate on these questions and establish their context. Each of the questions will then be examined in turn.

5.1 Context of the Questions

The data presented above show clearly that all three components of the electric field went to zero within the uncertainties less than a minute after the onset of the proton flux at the balloon. The central question is why did this occur? It is well known that the electric field inside a highly conducting object is zero. Is that what has happened here? Is the high conductivity preventing the balloon instrument from working, or, if working, bearing any relationship to the overlying ionospheric field? The overall process of understanding this event was initially focused on modeling the altitude profile of the conductivity changes. This modeling is finished, but is only valid above 20 km [K12]. The next section of the discussion will apply the model to the electric field mapping issue.

It will be shown in the next section that the data presented above are valid measurements of the ionospheric field. Why was the horizontal field so small? It is obvious that the flare and SEP events produced a major increase in ionospheric conductivity across the entire dayside. The perpendicular electric resistance of the ionosphere was reduced to a level far below normal. In effect, one could view the magnetosphere as having been shorted out. Is this concept valid? If so, what does shorting out the magnetosphere mean in practice?

Finally, we come to the jumps in the vertical electric field. It may not be immediately obvious to many readers why these features are so puzzling and important. In the stratosphere, the vertical electric field is an ohmic response to the air-earth current, which is in turn driven by large scale electrodynamic boundary conditions [*Bering*, 1995; *Bering et al.*, 1998; *Israel*, 1973; *Reiter*, 1992; *Roble and Tzur*, 1986]. In fair weather, the field is negative (downward) and relatively small. Large amplitude fluctuations and/or positive (upward) values of the stratospheric vertical electric field are usually the result of nearby electrified clouds, i.e. inclement weather. Thunderstorms are very rare over the Southern Ocean. In the absence of nearby thunderstorm activity, these jumps are unique and very puzzling, since there are no well-understood possible sources.

5.2 Effects Of The High Conductivity

Does the near-zero value of the electric field really represent atmospheric and magnetospheric conditions, or is it a localized ionospheric or instrumental artifact resulting from the high

conductivity? Addressing this question first required modeling what the upper atmospheric conductivity actually did during the event. K12 modeled the expected conductivity changes in the ionosphere and upper atmosphere during the SEP event. For the present purposes, the relevant results are the 0900 UT model curves presented in Figure 9D of K12.

The attenuation mapping of the fair weather horizontal electric field from the ionosphere to balloon altitude was originally studied by *Mozer and Serlin* [1969]. These calculations were repeated using the K12 0900 UT conductivity profile. The results of this calculation are shown in Figure 18. The curves shown in this figure are transmission functions. The abscissa is the wavelength in m, and the ordinate is the attenuation factor as a function of wavelength. The fact that the abscissa of this figure is in wavelength does not imply that the instrument measures wavelength. An attenuation factor of 1.0 implies perfect mapping. These curves illustrate the concept that the mapping of the horizontal electric field from the ionosphere to the balloon acts as a spatial low-pass filter. The solid curve plots the original result of *Ibid.*, while the dashed curve shows the attenuation factor recalculated using the 0900 UT model curve from Figure 9D of K12. The dashed curve is to the left of and above the solid curve, which means that the electric field measured by the balloon during the 2005 SEP event includes more of the short wavelength portion of the overlying ionospheric field than it would have under ordinary conditions. If the detector were shorted out by the conductivity enhancement, the dashed curve would lie to the right of and well below the solid curve. In sum, the detector was not shorted out by the conductivity enhancement; and therefore the very small measured horizontal field was probably an accurate representation of the overlying ionospheric field. To put it another way, the conductivity enhancement pushed the global circuit equipotentials down well below altitude of the balloon because the vertical global circuit current was maintained with a much smaller vertical field because of the enhanced conductivity.

5.3 Magnetospheric Response

What is the magnetospheric effect of the very high ionospheric conductivity? In the previous section, it was shown that the ionospheric convection plotted in Figure 11 was not the result of the conductivity shorting out the measurement. The data shown appear to be an accurate representation of the ionospheric electric field, at least in the vicinity of the balloon payload. What can be said about the global conditions at this time?

Figures 19 and 20 are plots of the IMAGE (Scandanavia) and CANMOS (Central Canada) magnetometer data for 20 January, 2005. Looking first at the IMAGE data in Figure 20, the magnetometer signals were very flat from about 0400 UT to 1345 UT at all stations except the four polar cap stations (NAL, LYR, HOR and BJN) which were in darkness all day at this point in the year. The ionospheric conductivity above these stations was probably not affected by the flare, since the Sun was not visible. The figure lacks the resolution to indicate if the actual drop in convection activity shown in Figure 19 is present in the magnetometer data or not. Certainly, the low level of magnetic perturbation is consistent with Figure 11, and indicated a global lack of convective activity. The wave activity seen at the highest latitudes probably accounts for the fact that K_p was not near 0 at this time, since K_p is a disturbance index.

Farther west, the Greenland and CANMOS data in Figures 15 and 20 were consistent with the IMAGE data in that there is no discernible convective activity for many hours before and after the flare. At this longitude and time of year, dawn was after 1200 UT, if it occurred at all (RES and CBB are Arctic stations), so the ionosphere above these stations was not illuminated by the flare. The wave activity seen from 0800 to 1200 UT in Figure 19 was confined to 1030-1200 UT in the Canadian sector.

The times of the second and third steps in the vertical component of the balloon electric field data are shown as vertical dashed lines in Figures 19 and 20. Both figures confirm the more detailed

results of Section 4.2.3 (Figures 16 and 17) that each of these steps occurred in coincidence with significant changes in ionospheric current flow. This coincidence suggests that the changes in the convection patterns shown in Figures 15, 19, and 29 were accompanied by large scale changes in the electrostatic potential in the ionosphere, which produced changes in the tropospheric vertical field. We will investigate this connection more in the next section.

An overall low level of convection was present prior to the flare and was consistent with the observed B_z northward, The response to the flare was to reduce the level of overall convection even more for several hours after the flare.

5.4 What caused the "steps" in E_{vert}?

The initial drop of E_{vert} to ~0 V/m at flare time appears to be the result of a large drop in the column resistance of the atmosphere caused by the ground level SEP event [*Holzworth et al.,* 1987]. The rest of this section will concentrate on the next two steps. In the previous section, magnetometer data from around the world indicated that the steps in the electric field were coincident with large scale changes in magnetospheric dynamics. As a first step in examining how this might have occurred, the Assimilative Mapping of Ionospheric Electrodynamics (AMIE) model was run for 20 January, 2005. AMIE assimilates magnetometer and radar data from around the world to infer an optimally constrained, least squares fit of the ionospheric electrostatic potential distribution, along with some related electrodynamic parameters [*Knipp et al.*, 1993; *Richmond et al.*, 1988; *Ridley et al.*, 2000]. A formerly available online IDL widget was used to run AMIE. This online model had a significant limitation. A standard statistical ionospheric conductivity model was used to estimate conductivity. Obviously, this standard conductivity model underestimated the conductivity in the aftermath of the flare and probably overestimated potential gradients.

The AMIE model produces contour maps of the inferred electrostatic potential in the ionosphere. Since electric field steps indicate abrupt changes in the ionospheric potential, Figures 21a&b show two minute intervals centered on the times that the jumps occurred in the balloon electric field data. Figure 21a indicates that the AMIE model indicates a doubling of the cross polar cap potential (CPCP) from 1354 to 1404 UT. These model plots show the Northern Hemisphere, so exact correspondence with the balloon data is not expected. Looking closely near the conjugate location to the balloon (1140 MLT, 60 geomagnetic latitude), the biggest changes occurred from 1358 to 1402 UT and have the right sign. The situation for the second jump is less clear. Figure 21b shows an abrupt increase in positive potential across the dayside at 1600 UT, which may correspond to the jump. However, there is also a strong negative change slightly poleward of the balloon location. It seems that the strongest conclusion one can reach from the AMIE results is that the model does not contradict the interpretation that the jumps in the balloon data indicate magnetospherically driven changes in the earth-ionosphere potential. These figures also give a ballpark estimate of the size of the expected changes in the Earth-ionosphere potential above the balloon payload. What the data are showing is that changes the vertical potential are concentrated in the atmosphere. So, our tentative explanation for jumps 2 and 3 seems to be that the change in the vertical field was caused by large scale changes in magnetospheric convection and ionospheric current flow.

The last step in the interpretation process is to ask if the K12 conductivity model is accurate enough to permit an assessment of the amount of change in ionospheric potential required to match the observations. This assessment requires one to estimate the vertical electric current density, j_z, and the Earth-ionosphere column resistance, R_h. The Earth-ionosphere potential drop is then found from $V_{iono} = j_z * R_h$. The current density was estimated using $j_z = E_{vert} * \sigma$.

R_h was estimated by height integrating the K12 Figure 9D conductivity models. Before the flare, the 0600 profile was used. After the flare, the 0900 profile was used, scaled to the observations at

the balloon. The big problem in this analysis is that the model is not valid below 20 km. This issue is unfortunate owing to the fact that the bulk of the column resistance was actually below 20 km. The 0600 model profile shows a scale height of ~10 km from 20-40 km, which is consistent with recent data [*Bering et al.*, 2003; *Bering et al.*, 2005]. In the same range, the 0900 profile shows a scale height of ~7 km, which also agrees with many other prior observations [*Byrne et al.*, 1988, *Ibid.*]. For want of a better scheme, both profiles were extended downward as smooth exponentials. Below the altitude where the profiles crossed, the 0600 profile was used. This approach gave an upper limit to R_h, and minimizes any flare effects.

The results of these calculations are shown in Figure 22, plotted as functions of Universal Time. From top to bottom, the three panels show R_h, j_z, and V_{iono}. The quiet time j_z is in reasonable agreement with expectation and prior observations. The post flare j_z is large and very variable but lies within the realm of prior observations. The inferred V_{iono} shown in the bottom panel is unreasonable and requires detailed comment. During the quiet time prior to the flare, Figure 22 shows that V_{iono} was inferred to have been ~-50 kV. Extensive prior work indicates that V_{iono} was normally ~-250 kV [*Markson and Kendra*, 1992]. There were three possible sources for the discrepancy, the lingering effect of enhanced conductivity owing to GLE 68 3 days earlier, a systematic error in E_{vert} owing to a shift in the zero level of the channel, or underestimation of R_h. It is, in fact, possible to adjust the zero level of the channel by an amount allowed by the known range of work function changes and produce an inferred $V_{iono} = -250$ kV prior to the flare. However, this adjustment makes the apparent voltages after 0700 UT much larger and has been ruled out. The discrepancy can also be resolved with an R_h~5 times larger than that inferred from K12 Figure 9D. That much change is certainly within the range of uncertainty in our extrapolation of the model.

After the flare, the inferred values of V_{iono} in the bottom panel of Figure 22 show approximately the variations one might expect from the AMIE results. However, the inferred fluctuations are an order of magnitude larger than AMIE suggests. This disagreement indicates that the post-flare value of R_h shown in the top panel of Figure 22 is at least an order of magnitude too large. While this conclusion is intuitively reasonable, given the radiation environment, we are unaware of an appropriate model to apply to study this question further.

5.4.1 What was the role of proton cutoff variations? *Kokorowski et al.* [2006] suggested that the electric field jumps at 1400 and 1556 UT could be caused by rapid changes in geomagnetic cutoffs resulting in increased precipitation at lower latitudes and therefore changes in conductivity. We revisit this possibility by constructing a global picture of solar proton behavior from observations at multiple altitudes (geostationary orbit (GEO), Global Positioning Satellite (GPS) orbit, and low-earth polar orbit (LEO)) in the context of solar wind and geomagnetic variability.

On this day, ACE SWEPAM solar wind plasma data were not available after 0653 UT and Wind data were not available after 0703. Therefore, we calculate dynamic pressure from ACE SWICS [*Gloeckler et al.*, 1998] twelve-minute proton number density and bulk speeds and one-hour alpha particle (He^{2+}) number density and bulk speeds. The He^{2+} quality flags indicate good data on this day; a few of the proton data points are fill values. After the He^{2+} data are interpolated to the proton data times (adjusting both sets of time stamps to the centers of the sample intervals), solar wind dynamic pressure (P_{dyn}) is calculated from the proton and helium data. The bulk proton speed v_p reached a peak of 886 km/s at 1106 UT (unshifted), then decreased steadily to 580 km/s by the end of 20 January 2005. Between 1305 and 1330, the proton density increased from 0.28 to 2.9 cm^{-3} (with a data gap in between) and reached a peak of 4.4 cm^{-3} at 1354 UT. As a result, P_{dyn} increased from 0.55 to 3.8 nPa (v_p at the jump is 844 km/s), reaching a maximum of 5.1 nPa at 1400 UT (1429 shifted, Figure 23a). The ACE 1-s magnetic field data (Smith et al. 1998) indicate a rapid southward IMF rotation (nearly in the GSE X-Z plane) between 1317 and 1318 UT (not shown). The density increase and this field rotation may have been signatures of the same plasma structure. Assuming a phase front normal to the velocity and using the velocity at the increase, the travel time from ACE

to the magnetopause was approximately 27 minutes, and the arrival time was 1345 UT. The SYM-H index increased from -28 to -16 nT between 1344 and 1355 UT (Figure 23b). The SYM-H increase may have been the signature of a weak compression by the P_{dyn} increase. Therefore, the arrival time is bounded between 1345 and 1355 UT. The AL index decreased from -80 to -310 nT between 1355 and 1357 UT, after the first current burst was observed at MINIS (Figure 23b). This timing suggests that the arrival of the pressure pulse resulted in the first electric field jump and the small increase in auroral activity.

Dynamic pressure enhancements cause increases in eastward-observed GOES solar proton fluxes, which have gyro centers inside GEO [*Rodriguez et al.,* 2010]. Such increases indicate decreases in geomagnetic cutoff latitudes inside GEO. For $P_{dyn} < 10$ nPa, eastward-observed GOES solar proton fluxes generally have a lower magnitude than westward-observed fluxes due to geomagnetic cutoff effects on the former [*Rodriguez et al.*, 2014]. Figure 23c shows fluxes from the GOES-10 (eastward) and -12 (westward) P1 (0.74-4.2 MeV) and P3 (8.7-14.5 MeV) channels, the former characterized by the injections of lower-energy geomagnetically-trapped protons, as discussed earlier, and the latter representative of solar proton behavior. The GOES-10 P3 fluxes increased sharply by 1355 UT, the time of the first MINIS current burst, indicating that the effect of the P_{dyn} increase had reached GEO by this time. They did not reach the level of the GOES-12 fluxes, consistent with P_{dyn} being less than 10 nPa. The GOES-10 P3 fluxes increased gradually prior to the MINIS current burst at 1554 UT and prior to the injection observed by GOES-10 P1. This behavior was characteristic of solar proton behavior during the substorm growth phase prior to a particle injection and consistent with the enhanced AL index [*Rodriguez,* 2012].

Proton observations from the GPS Combined X-ray Dosimeter (CXD) can be used to observe geomagnetic cutoff variations down to L = 4 [*Cayton et al.*, 2007; *Chen et al.*, 2020]. The CXD produces a total of five integral proton rates [*Cayton et al.*, 2004] from which proton integral and differential proton fluxes have been inverted [*Morley et al.*, 2017; *Carver et al.*, 2018]. During January 2005, CXD data were available from five GPS satellites (ns54, ns56, ns59, ns60, ns61). As a result, coverage was sparse compared to later SEP events in 2012 and 2017 [*Chen et al.*, 2020]. Nonetheless, the CXD data provide key insight into cutoff variations vs. L during this period. Due to an increase in MeV electron fluxes from January 19 through January 21, electron contamination is present in the P3 rate below L = 5 [*Cayton et al.*, 2007], where proton cutoff variations are expected. By inspection, this contamination affects at least three of the derived integral fluxes reported in the GPS data files. Therefore, for this paper, we use two of the uncontaminated channel rates, one low energy (P2, >10 MeV) and one high energy (P4, >57 MeV) [*Carver et al.*, 2018]. An upper envelope defined by the greatest rate in each 4-minute period among all satellites exhibits the gradual decrease and some of the variations observed at GOES (e.g., 1345-1400 UT) and no deep dropouts from cutoffs (Figure 23d). Therefore, this envelope provides a reliable estimate of the near-Earth interplanetary rate for normalization of the rates. The cutoff location is defined as the point at which the observed rate is half the envelope rate [*Mazur et al.*, 1999]. The observed cutoffs are expressed in terms of McIlwain L calculated in the T89 external field [*Tsyganenko*, 1989] and IGRF internal field model. They are indicated (for P2) by circles in Figure 23d and summarized in Table 1. Differences between P2 and P4 cutoffs are small. With a smaller lower energy threshold, P2 cutoffs could be expected to be at a higher latitude. However, since P2 has a three-orders-of-magnitude greater response at 60 MeV than at 10 MeV [*Carver et al.*, 2018], its geomagnetic cutoff response may be dominated by higher energies. The largest cutoff change occurred between 14:10 and 15:05 UT ($\Delta L = -0.5$ in P2), observed by ns56 between 14.4 and 15.2 MLT, following two hours during which the cutoffs were steady within $\Delta L = 0.2$ (Figure 23e). This response to the P_{dyn} increase was much more gradual than the response observed in GEO.

Because there were no CXD observations at low L during the second electric field jump, we also examine solar proton observations from the NOAA 15, 16 and 17 Polar Orbiting Environmental

Satellites (POES). We use fluxes from the MEPED P5 channel (2.5-7.0 MeV), which has a sharp factor-of-50 upper energy cutoff and is free of electron contamination [*Yando et al.*, 2011]. Because solar proton fluxes in the polar cap can be highly structured [*Scholer*, 1972; *Blake et al.*, 2001], cutoff locations are determined where the P5 flux is half the average of the fluxes observed above L = 7 (McIlwain L calculated in the International Geomagnetic Reference Field [*Finlay et al.*, 2010]. In Figure 1f, cutoff locations are distinguished by satellite and by magnetic local time sector (night: 21-03, dawn: 03-09, day: 09-15, dusk: 15-21). These L values were greater than those observed in the CXD rates due to the lower energies and narrower energy response of MEPED P5. Cutoffs on the dayside tend to be at greater L than on the nightside [*Paulikas et al.*, 1968]. Cutoffs increased in L slightly before the arrival of the P_{dyn} increase, then decreased by ~0.8L (dusk/night) over 16 min between 1354 (L=5.8) and 1411 (L=5.0). The cutoff L decrease on the dayside was more gradual, about the same duration as the cutoff change observed by GPS ns56 post-noon. The similar dayside cutoffs observed by N17 at 1354 (L=6.6) and N16 at 1357 (L=6.5) also indicate that the cutoffs did not change rapidly at the time of the first MINIS current burst. A more gradual cutoff response in LEO than in GEO to a P_{dyn} increase has been observed before [*Rodriguez et al.*, 2014].

During this period, the MINIS balloon was near L = 4 and was equatorward of the 140 MeV cutoff location, based on observations by the POES MEPED omnidirectional detectors [*K12*]. Conductivity modeling results were consistent with 150 and 200 MeV proton precipitation [*Ibid.*]. The cutoffs observed in the MEPED 2.5-7.0 MeV fluxes and in the GPS CXD >10 MeV and >57 MeV rates were at greater L values and at lower energies. Although not at the MINIS location, the combined GOES, POES (P5) and GPS solar proton observations provide a global picture of cutoff dynamics. The CXD and MEPED observations suggest that, while there was a cutoff change following the MINIS current burst at 1355, it was much more gradual than the current burst. Therefore, the first current burst and the cutoff change both may have resulted from the compression of the magnetosphere by the P_{dyn} increase. In contrast, at the time of the MINIS current burst at 1554, there was no significant cutoff change. The current burst was associated with an increase in magnetospheric convection, indicated by an increase in auroral activity (AL index) and the proton injection observed by GOES-10 P1, both of which were larger than at the time of the first current burst.

5.5 Further Discussion of Questions that Remain

5.5.1 Why have we never seen this before? We may have seen it before. It is hard to know. This event is only the second time when we have made balloon E observations during a post flare event where the ordinary fair weather field has been shorted out. Usually, the fair-weather Earth ionosphere potential drop is 250 kV, so 50kV ionospheric potentials are only 20% of the signal and much less noticeable. In addition, thunderstorms can turn on quickly, so abrupt changes in vertical field are usually attributed to unknown changes in distant weather systems. See, for example, the vertical field data for another major geomagnetic storm reported by *Bering et al.* [1991].

5.5.2 Can we understand isolated sharp changes? It is a textbook result in plasma physics that high conductivity has the effect of narrowing current sheet boundary thicknesses between different regions [*Chen*,1974]. We may have observed two examples of this effect. The real surprise is the rarity of such observations.

5.5.3 Why don't we see large horizontal fields during the 2nd and 3rd steps? The expection that there should be large horizontal fields during the steps is based on the assumption that a spatial boundary in the ionosphere was moving past overhead. In this model, vertical displacement of the electric equipotential surfaces between regions necessarily produces horizontal fields.

However, the existence of data from three extensive magnetometer networks affords us the opportunity to disambiguate the data. Since there was very little geographic dispersion of the timing

in the associated magnetic perturbations, the events occurred simultaneously within 1-5 minutes over large regions. Thus, the events seen by the balloon payload were temporal variations. This model does not require horizontal fields because we were not at a spatial boundary. The vertical electric field in the stratosphere is an ohmic response to the current flowing in the global circuit. It is the result of local space charge accumulation [*Haldoupis et al.,* 2017]. Vertical field variations are, therefore, the result of vertical charge transport, which should have been downward in this situation. The data gaps obscure the situation. There were negative vertical field perturbations during the step intervals that correspond to bursts of downward current, consistent with this expectation.

A detailed plot of the second step (reminder, the first one occurred right at the flare and is understood) is shown in Figure 24. A couple of cautions are in order in viewing the figure. First, the spin period was ~40 s, so the prominent sine waves in the horizontal components at 1355-1358 and 1402-1405 are spin residuals owing to dc offset issues with the despin. In order to despin the horizontal field data correctly, one must first subtract the spin averaged dc value of the data. In normal processing, the code uses a 5-minute moving sine wave fit to obtain this average. During the intervals shown in Figures 24 and 25, the missed-phone-call data gaps and the extreme variations turn the fits into nonsense. Therefore, the middle part of this Figure uses the 1349-1354 fit for the dc average. The fast current bursts that occurred at ~1355 and ~1402 produced common mode offsets that took about 3 minutes to decay, as shown by the spin residuals.

Second caution, the calibration/conductivity measurement cycles (cal-cycles) took place every 10 minutes. Those data were marked by a flag bit in the telemetry stream and excluded from this plot. The small data gaps at ~1355 and ~1405 are the result of this exclusion. The long gap between the disturbances was a dropped IRIDIUM telemetry phone call.

The horizontal field data were briefly compromised by the spin residuals. In the case of both disturbances, it appears there was a ~70 mV/m SW/NE bipolar perturbation pulse that had a shorter period than 40 s. There does not appear to be any evidence that there was a net horizontal field.

The vertical field data were much more useful. The initial fast variation burst was followed by a small, ~-0.1 V/m dc shift. By the end of the data gap the field had risen to nearly zero. Right after the gap, there was positive pulse of a few seconds duration followed by a ~-0.2V/m negative excursion of nearly two minutes duration. This excursion indicates there was a downward current that was consistent with the fact that shifts in the vertical field require removing the local space charge that was generating the vertical field.

Figure 25 presents the data taken during the third step. This figure also shows two calibration/ conductivity-measurement cycle (cal-cycle) gaps in the plot, at ~1555 and ~1605. There was also a dropped phone call data gap in the middle. There was a fast variation burst at the start of the step prior to the 1555 cal-cycle gap. The event is barely noticeable in the horizontal field data, which show no minute scale horizontal field perturbations at all. The vertical field data were off-scale for the low gain TM channels during the few seconds between the start of the event and the cal cycle. It was back on scale at the end of the cal cycle. Again, we observed ~ 2 min of strong negative field and therefore, downward current. The previous comment about charge removal applies here, too.

6. Conclusions

Does the near-zero value of the electric field really represent atmospheric and magnetospheric conditions, or is it a localized ionospheric or instrumental artifact resulting from the high conductivity?

We have shown that the detector was not shorted out by the conductivity enhancement; and therefore the very small measured horizontal field was an accurate representation of the overlying ionospheric field.

Conversely, what is the magnetospheric effect of the very high ionospheric conductivity?

The overall low level of convection was present prior to the flare and was consistent with the observed *Bz* northward, The response to the flare was to reduce the convection activity even more for several hours.

What caused the jumps in the vertical electric field?

It appears very likely that the first drop to 0 of E_{vert} was a simple shorting out of the global circuit. The next two steps in E_{vert} appear to have been responses to abrupt changes in magnetospheric convection.

Acknowledgments. The MINIS campaign was funded by the National Science Foundation of Polar Programs and Atmospheric Sciences Division. We thank our South African support, which included many people from both SANAP and DEAT. We also thank the folks at CSBF for help in test launching from McMurdo in 2003. We thank all of the institutes who maintain the IMAGE, CANOPUS, CANMOS and Greenland magnetometer arrays. The magnetometer data can be found at the websites of these arrays. Portions of this work was supported under NSF grants ATM-0233370 and OPP-0230441. Other portions of this work were funded by the National Science Foundation under grant numbers: ATM-0408356, ATM-0649706 and ATM-0649489. A portion of this work was supported by NSF award AGS-1024701 to the University of Colorado. John Sample's efforts were supported through the NSF Graduate Research Fellowship Program. We thank the CXD team at Los Alamos National Laboratory for processing the CXD data and making it available to the public (v1.08): https://ngdc.noaa.gov/stp/space-weather/satellite-data/satellite-systems/gps/. The POES 16-s CDFs are available from NOAA NCEI: https://ngdc.noaa.gov/stp/satellite/poes/dataaccess.html. The GOES data are available from NOAA NCEI: https://ngdc.noaa.gov/stp/satellite/goes/dataaccess.html. We thank the ACE SWICS and MAG instrument teams and the ACE Science Center for providing the ACE Level 2 data. MINIS data are available at http://gc.phys.uh.edu/data/Other_UH_Experiments/MINIS/ .

The Editor thanks (for JGR-A manuscripts only)…

References

Baker, D., R. Belian, P. Higbie, and E. Hones Jr (1979), High-energy magnetospheric protons and their dependence on geomagnetic and interplanetary conditions, *Journal of Geophysical Research: Space Physics*, *84*(A12), 7138-7154.

Bering, E. A., III (1995), The global circuit: Global thermometer, weather by-product, or climatic modulator?, *Rev. Geophys.*, *33*(U. S. National Report to International Union of Geodesy and Geophysics), 845-862.

Bering, E. A., III, J. R. Benbrook, G. J. Byrne, R. H. Holzworth, and S. P. Gupta (2003), Long term changes in the electrical conductivity of the stratosphere, *Adv. Space Res.*, *32*(9), 1725-1735.

Bering, E. A., III, J. R. Benbrook, R. Haacke, J. R. Dudeney, L. J. Lanzerotti, C. G. Maclennan, and T. J. Rosenberg (1991), The intense magnetic storm of December 19, 1980: Observations at L=4, *Journal of Geophysical Research*, *96*(A4), 5597-5617.

Bering, E. A., III, J. R. Benbrook, R. H. Holzworth, G. J. Byrne, and S. P. Gupta (2005), Latitude gradients in the natural variance in stratospheric conductivity - implications for studies of long term changes, *Adv. Space Res.*, *35*, 1385-1397.

Bering, E. A., III, A. A. Few, and J. R. Benbrook (1998), The global circuit, *Physics Today*, *51*(10), 24-30.

Bering, E. A., III, et al. (2005), Balloon observations of temporal and spatial fluctuations in stratospheric conductivity, *Adv. Space Res.*, *35*, 1434-1449.

Blake, J., M. McNab, and J. Mazur (2001), Solar-proton polar-cap intensity structures as a test of magnetic field models, *Adv. Space Res.*, *28*(12), 1753-1757.

Byrne, G. J., J. R. Benbrook, E. A. Bering, III, D. M. Oro, C. O. Seubert, and W. R. Sheldon (1988), Observations of the stratospheric conductivity and its variation at three latitudes, *Journal of Geophysical Research*, *93*, 3879-3892.

Carver, M. R., J. P. Sullivan, S. K. Morley, and J. V. Rodriguez (2018), Cross calibration of the GPS constellation CXD proton data with GOES EPS, *Space Weather*, *16*(3), 273-288.

Cayton, T., R. Friedel, A. Varotsou, J. Sullivan, and S. Young (2007), Multi-satellite SEP observations by the GPS energetic particle detector constellation, in *AGUFM*, edited, pp. SM23C-03.

Cayton, T. E. (2004), Monte carlo simulation of the particle channels of the combined x-ray sensor and dosimeter (CXD) for GPS block IIR and block IIF, Tech. Rep. LA-UR-04-7092, Los Alamos Natl. Lab., Los Alamos, N.M.

Chen, F. F. (1974), *Introduction to Plasma Physics*, Plenum Press, New York.

Chen, Y., S. K. Morley, and M. R. Carver (2020), Global Prompt Proton Sensor Network: Monitoring Solar Energetic Protons based on GPS Satellite Constellation, *Journal of Geophysical Research: Space Physics*, *125*(3), e2019JA027679.

Finlay, C. C., S. Maus, C. Beggan, T. Bondar, A. Chambodut, T. Chernova, A. Chulliat, V. Golovkov, B. Hamilton, and M. Hamoudi (2010), International geomagnetic reference field: the eleventh generation, *Geophysical Journal International*, *183*(3), 1216-1230.

Gloeckler, G., J. Cain, F. Ipavich, E. Tums, P. Bedini, L. Fisk, T. Zurbuchen, P. Bochsler, J. Fischer, and R. Wimmer-Schweingruber (1998), Investigation of the composition of solar and interstellar matter using solar wind and pickup ion measurements with SWICS and SWIMS on the ACE spacecraft, in *The advanced composition explorer mission*, edited, pp. 497-539, Springer.

Haldoupis, C., M. Rycroft, E. Williams, and C. Price (2017), Is the "Earth-ionosphere capacitor" a valid component in the atmospheric global electric circuit?, *J. Atmos. Solar Terr. Phys.*, *164*, 127-131.

He, J., and J. V. Rodriguez (2018), Onsets of Solar Proton Events in Satellite and Ground Level Observations: A Comparison, *Space Weather*, *16*(3), 245-260, doi:10.1002/2017sw001743.

Holzworth, R. H., and E. A. Bering, III (1996), Ionospheric electric fields from stratospheric balloon borne probes, in *Space Physics Instrumentation: What Works and What Doesn't*, edited by J. Borovsky and R. Pfaff, American Geophysical Union, Washington, DC.

Israel, H. (1973), *Atmospheric Electricity*, 2nd ed., Natl. Tech. Inform. Serv., U. S. Dept. Commerce, Springfield, Virginia.

Knipp, D. J., et al. (1993), Ionospheric convection response to slow, strong variations in a northward interplanetary magnetic field: A case study for January 14, 1988, *Journal of Geophysical Research: Space Physics*, *98*(A11), 19273-19292, doi:10.1029/93ja01010.

Kokorowski, M., et al. (2008), Magnetospheric electric field variations caused by storm-time shock fronts, *Adv. Space Res.*, *42*, 181-191.

Kokorowski, M., et al. (2006), Rapid fluctuations of stratospheric electric field following a solar energetic particle event, *Geophys. Res. Lett.*, *33*, L20105.

Kokorowski, M., A. Seppälä, J. G. Sample, R. H. Holzworth, M. P. McCarthy, E. A. Bering, and E. Turunen (2012), Atmosphere-ionosphere conductivity enhancements during a hard solar energetic particle event, *Journal of Geophysical Research: Space Physics*, *117*(A5), n/a-n/a, doi:10.1029/2011ja017363.

Markson, R., and D. Kendra (1992), Ionospheric potential measurments at Hawaii and Christmas Island, in *Proceedings 9th International Conference on Atmospheric Electricity*, edited by E. Borisenkov and V. Stepanenko, p. 18, A.I. Voeikov Main Geophysical Observatory, St. Petersburg, Russia.

Mazur, J., G. Mason, M. Looper, R. Leske, and R. Mewaldt (1999), Charge states of solar energetic particles using the geomagnetic cutoff technique: SAMPEX measurements in the 6 November 1997 solar particle event, *Geophys. Res. Lett.*, *26*(2), 173-176.

Mewaldt, R., M. Looper, C. Cohen, G. Mason, M. Desai, D. Haggerty, A. Labrador, R. Leske, J. Mazur, and E. Stone (2005), Space Weather Implications of the 20 January 2005 solar energetic particle event, paper presented at AGU Spring Meeting Abstracts.

Millan, R. M. (2011), Understanding relativistic electron losses with BARREL, *J. Atmos. Solar Terr. Phys.*, *73*(11–12), 1425-1434, doi:http://dx.doi.org/10.1016/j.jastp.2011.01.006.

Millan, R. M., et al. (2005), Global monitoring of relativistic electron precipitation with balloon networks: MINIS and beyond, *EOS, Trans. AGU*, *86*(56), Abstract SM51D-04.

Morall, H., K. G. McKracken, C. C. Schoeman, and P. Stoker (2005), The ground level enhancements of 20 January 2005 and 28 October 2003, paper presented at 29th International Cosmic Ray Conference, Pune, India.

Morley, S., J. Sullivan, M. Carver, R. Kippen, R. Friedel, G. Reeves, and M. Henderson (2017), Energetic particle data from the global positioning system constellation, *Space Weather*, *15*(2), 283-289.

Mozer, F. S., and R. Serlin (1969), Magnetospheric electric field measurements with balloons, *Journal of Geophysical Research*, *74*, 4739.

Paulikas, G., J. Blake, and S. Freden (1968), Low-energy solar-cosmic-ray cutoffs: Diurnal variations and pitch-angle distributions, *Journal of Geophysical Research*, *73*(1), 87-95.

Plainaki, C., A. Belov, E. Eroshenko, H. Mavromichalaki, and V. Yanke (2007), Modeling ground level enhancements: Event of 20 January 2005, *Journal of Geophysical Research: Space Physics*, *112*(A4).

Reiter, R. (1992), *Phenomena in atmospheric and environmental electricity*, Elsevier Science Publishers B.V., Amsterdam.

Richmond, A. D., et al. (1988), Mapping electrodynamic features of the high-latitude ionosphere from localized observations: Combined incoherent-scatter radar and magnetometer measurements for January 18--19, 1984, *Journal of Geophysical Research*, *93*, 5760.

Ridley, A. J., G. Crowley, and C. Freitas (2000), An empirical model of the ionospheric electric potential, *Geophys. Res. Lett.*, *27*(22), 3675-3678, doi:10.1029/1999gl011161.

Roble, R. G., and I. Tzur (1986), The global atmospheric-electrical circuit, in *The Earth's Electrical Environment*, edited, National Academy Press, Washington, D.C.

Rodriguez, J. (2012), Undulations in MeV solar energetic particle fluxes in Earth's magnetosphere associated with substorm magnetic field reconfigurations, *Journal of Geophysical Research: Space Physics*, *117*(A6).

Rodriguez, J., J. Krosschell, and J. Green (2014), Intercalibration of GOES 8–15 solar proton detectors, *Space Weather*, *12*(1), 92-109.

Rodriguez, J., T. Onsager, and J. Mazur (2010), The east-west effect in solar proton flux measurements in geostationary orbit: A new GOES capability, *Geophys. Res. Lett.*, *37*(7).

Rodriguez, J., I. Sandberg, R. Mewaldt, I. Daglis, and P. Jiggens (2017), Validation of the effect of cross-calibrated GOES solar proton effective energies on derived integral fluxes by comparison with STEREO observations, *Space Weather*, *15*(2), 290-309.

Scholer, M. (1972), Polar-cap structures of solar protons observed during the passage of interplanetary discontinuities, *Journal of Geophysical Research*, *77*(16), 2762-2769.
Smith, C. W., J. L'Heureux, N. F. Ness, M. H. Acuna, L. F. Burlaga, and J. Scheifele (1998), The ACE magnetic fields experiment, in *The advanced composition explorer mission*, edited, pp. 613-632, Springer.
Tsyganenko, N. A. (1989), A magnetospheric magnetic field model with a warped tail current sheet, *Planetary and Space Science*, *37*(1), 5-20.
Yando, K., R. M. Millan, J. C. Green, and D. S. Evans (2011), A Monte Carlo simulation of the NOAA POES medium energy proton and electron detector instrument, *Journal of Geophysical Research: Space Physics*, *116*(A10).

Mailing addresses:

Edgar A. Bering III, University of Houston Physics Dept., 3507 Cullen Blvd. #617, Houston, TX 77005

Robert H. Holzworth, Michael P. McCarthy, Department of Earth and Space Sciences, University of Washington, Johnson Hall Rm-070, Box 351310, 4000 15th Avenue NE, Seattle, WA 98195-1310

Michael Kokorowski, Jet Propulsion Laboratory, 4800 Oak Grove Dr., Pasadena, CA 91109

Robyn M. Millan, Leslie Woodger, Dartmouth College, Physics Dept., 244 Wilder Hall, Hanover, NH 03755

Juan V. Rodriguez, Ball Aerospace, 1600 Commerce St., Boulder, CO 80301

John G. Sample, Montana State University, Department of Physics, PO Box 173840, Bozeman, MT 59717-3840

David M. Smith, UC Santa Cruz, Physics Department, 1156 High Street, Santa Cruz, CA 95064

Table 1. Summary of cutoff times and locations (UT and T89 L) observed in GPS CXD P2 and P4 rates between 1200 and 1800 UT on 20 January 2005.

P2 UT	P2 T89 L	P4 UT	P4 T89 L	Satellite
12:19	4.79	12:21	4.83	ns59
12:29	4.78	12:31	4.74	ns60
13:14	4.80	13:13	4.77	ns54
13:20	4.99	13:21	5.01	ns61
13:43	4.99	13:43	4.99	ns56
14:10	4.88	14:08	4.84	ns60
15:05	4.38	15:07	4.41	ns56
17:04	5.08	17:08	4.96	ns54
17:22	4.68	17:18	4.75	ns59
17:54	4.72	17:57	4.67	ns61

Figure 1. Summary plot of GOES SEM data from January 15-23, 2005. From top to bottom panels show GOES 12 solar X-rays, GOES 12 electrons and GOES 11 Protons and alpha particles, GOES 12 total magnetic field, and McMurdo Neutron Monitor counting rate (figure by Daniel Wilkinson of the NOAA National Centers for Environmental Information).

Figure 2. IMF observed by ACE for week starting 16 January 2005. Field components in GSM coordinates.

Figure 2. Solar wind density and velocity observed by ACE for the same interval as Figure 2.

Figure 4. Detail of Figure 2 for 20 January 2005.

Figure 5. ACE SWICS velocity and density data for 20 January 2005.

Figure 6. Two magnetic indices during the two week interval containing MINIS flight 2S. Top panel depicts K_p and the bottom panel depicts D_{st}.

Figure 7. *AE* index on 20 January 2005.

Figure 8. Top panel is top left panel of Figure 1 from *Moraal et al.* [2005], showing the three peaks seen by the SANAE neutron monitor during the GLE of 20 January 2005. Bottom panel is the bottom left panel of Figure 2 in *He and Rodriguez* [2018].Time series of normalized 1 min count rates from neutron monitors (NMs) and GOES 10 EPS and HEPAD channels, as well as 1 min >100 MeV integral fluxes (on the right axes in red). The event onset times detected by each instrument are indicated by a dashed black line, and the event onset times detected in the >100 MeV integral flux data are indicated by a red dotted line. For clarity, only select NMs are shown in the plot.

Figure 9. Top three panels present the three components of the electric field in Earth-fixed geomagnetic coordinates. Bottom panel is an energy-time spectrogram from the MINIS X-ray detector for 40 minutes at the time of the X7.1 solar flare on 20 January 2005.

Figure 10. Comparison of GOES and balloon data from the 20 January 2005 flare. Panel (a) at the top of the figure shows 1 min averages of the vertical electric field measured by MINIS Flight 2S for all of 20 January 2005. Panel 10(b), second from top, shows the negative ion conductivity measured by the relaxation technique. Panel 10(c) , third from the top, shows the energetic particle data from GOES 11. Panel 10(d), shows magnetometer data from the GOES 12 geosynchronous spacecraft.

Figure 11 shows the horizontal electric field data plotted as equivalent ionospheric convection in clockdial format. The view is down on the South Pole, which makes the clockface correspond to a normal clock. The outer ring gives the magnetic local time, The inner ring shows the UTC of the observations, with the UTC-MLT conversion fixed at the start of the interval shown. The bar between the rings shows the geomagnetic latitude. The base of each one min average data arrow is at the location of the balloon at the indicated UTC. The arrow represents the ionospheric flow velocity vector.

Figure 12. Despun balloon electric field observations plotted in earth-fixed geomagnetic coordinates using a 1 Hz sample rate. From top to bottom, the panels show the vertical field at two gains, poleward, and eastward components. The four-hour interval shown exhibits the 2nd and 3rd step-like changes in the vertical field.

Figure 13. GOES 0.6-4 MeV proton fluxes plotted as a function of UTC for the same interval as Figure 12. Top to bottom, the panels show data from GOES 12, GOES 11, and GOES 10, plotted in East to West order.

Figure 14. Some data taken in 1650. A map of Canada, showing magnetometer observatories (green dots), GOES conjugate footprints (cyan circles) and balloon conjugate track (red line).

Figure 15. Magnetometer data from the west coast of Greenland during 20 January 2005.

Figure 16. Magnetometer X component from the stations located in Figure 14 plotted vs. UTC for the time interval of Figures 12 and 13.

Figure 17. Magnetometer Y component from the same stations and interval as Figure 16.

Figure 18. The attenuation factor or transfer function that maps the ionospberic electric field to balloon altitude is plotted as a function of ionospheric electric field wavelength.

Figure 19. Magnetometer data from the IMAGE network in Scandinavia during 20 January 2005.

Figure 20. Magnetometer data from the CANMOS network in Canada during 20 January 2005.

Figure 21 a & b. Models of the Northern Hemisphere ionospheric potential patterns computed by AMIE plotted at 2 minute intervals at the time of the 2nd and 3rd steps.

Figure 22. Top to bottom, height integrated column resistance, vertical current density and Earth-ionosphere potential, inferred as described in the text; all plotted as functions of time.

Figure 23. Vertical lines at 1355 and 1554 indicate the times of current bursts observed at MINIS. (a) Solar wind dynamic pressure calculated from ACE SWICS proton and alpha particle density and velocity, shifted by the solar wind travel time to the magnetopause. (b) WDC Kyoto 1-min SYM-H and provisional AL indices. (c) GOES-10 and -12 0.7-4.2 MeV and 8.7-14.5 MeV proton fluxes. (d) Upper envelope of CXD P2 rates (>10 MeV protons) from the five GPS satellites, an estimate of the near-Earth interplanetary solar proton rates level. (e) CXD P2 rates normalized to the upper envelope as a function of time and T89 McIlwain L shell. Open circles indicate cutoff locations, where P2 rates are attenuated to half the interplanetary level. In two cases (c. 1300-1330 and c. 1700-1800), two satellite traces overlap and there are two open circles in close succession, one of which corresponds to the obscured trace. (f) POES MEPED 90-deg telescope P5 cutoffs. Triangles = N15, diamonds = N16, circles = N17.

Figure 24. Three components of the electric field in Earth-fixed geomagnetic coordinates plotted at a 1Hz sample rate as a function of UTC. The vertical field is shown at two gains.

Figure 25. Three components of the electric field in Earth-fixed geomagnetic coordinates plotted at a 1Hz sample rate as a function of UTC. The vertical field is shown at two gains.

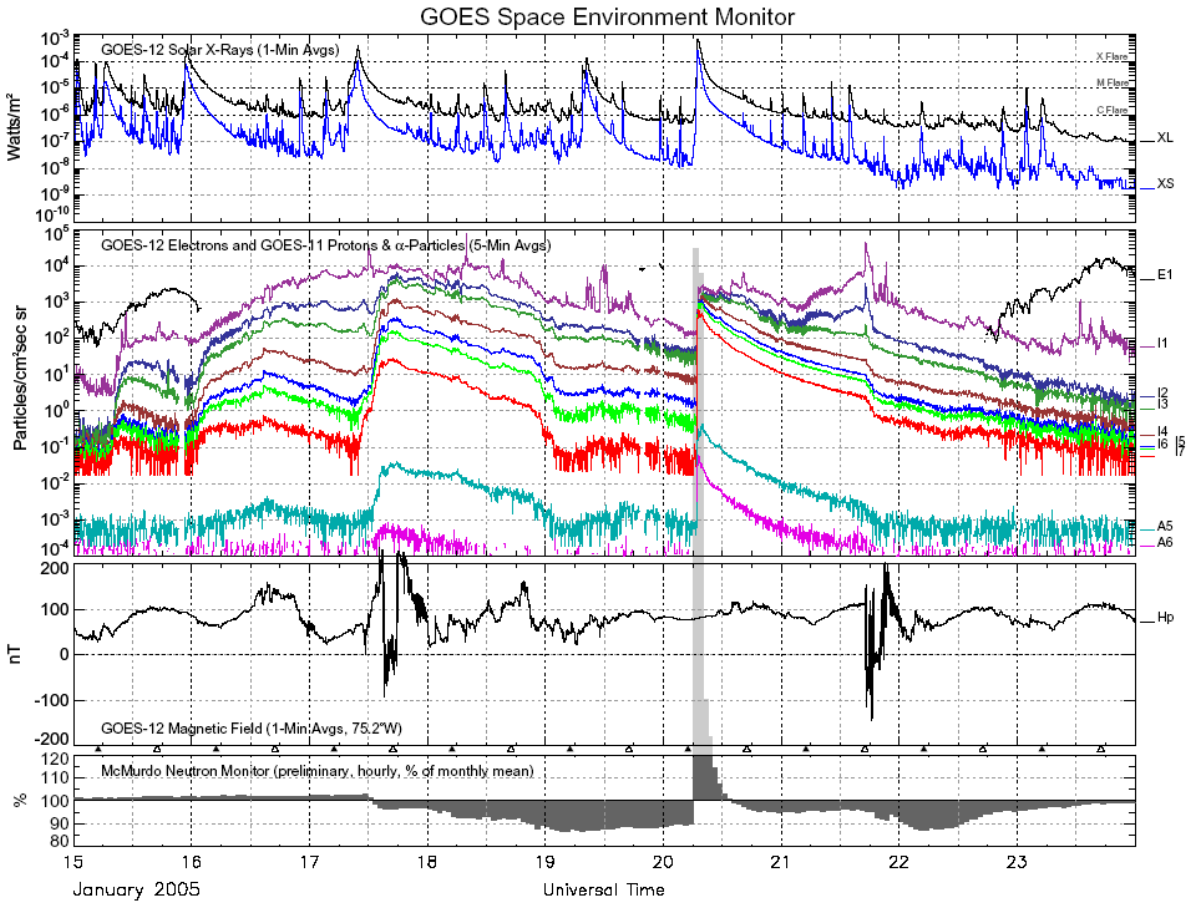

Figure 1. Summary plot of GOES SEM data from January 15-23, 2005. From top to bottom panels show GOES 12 solar X-rays, GOES 12 electrons and GOES 11 Protons and alpha particles, GOES 12 total magnetic field, and McMurdo Neutron Monitor counting rate (figure by Daniel Wilkinson of the NOAA National Centers for Environmental Information).

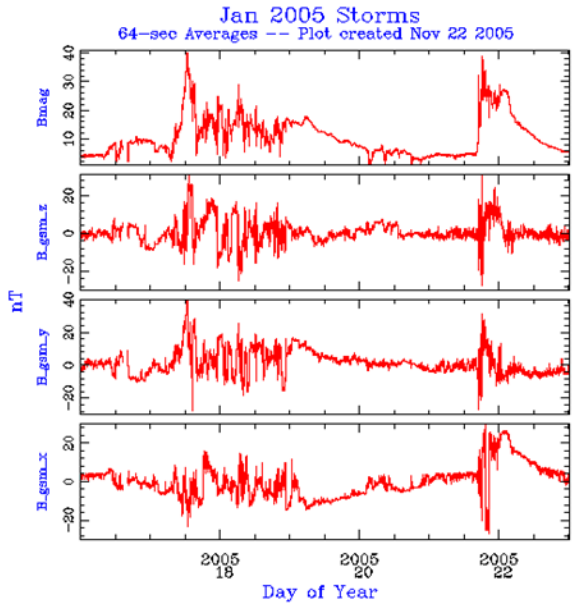

Figure 2. IMF observed by ACE for week starting 16 January 2005. Field components in GSM coordinates.

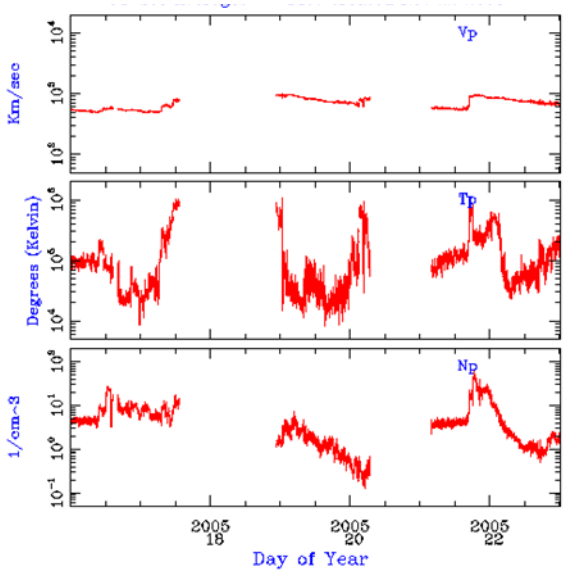

Figure 3. Solar wind density and velocity observed by ACE for the same interval as Figure 2.

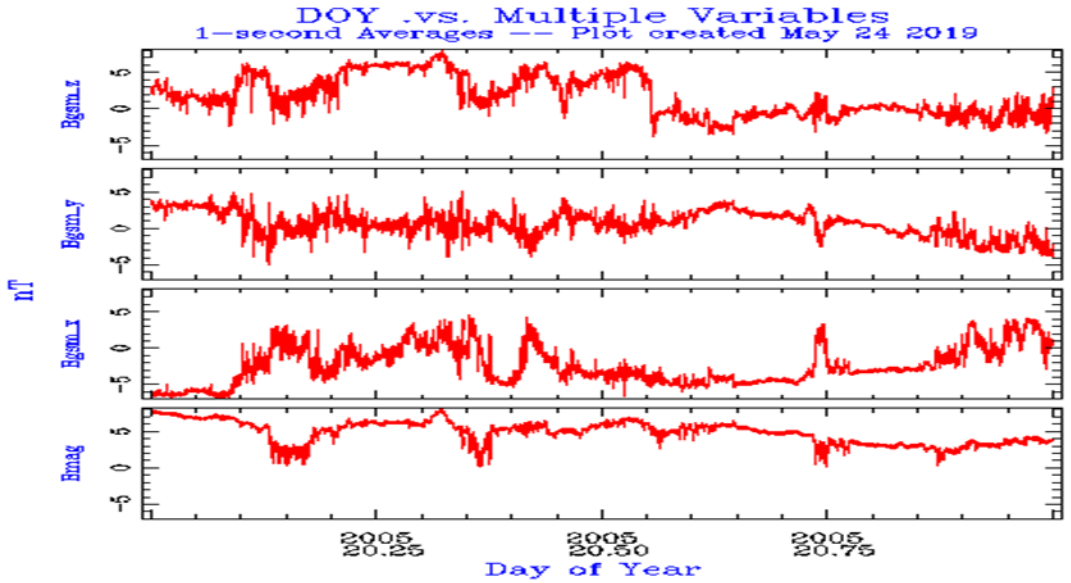

Figure 4. Detail of Figure 2 for 20 January 2005.

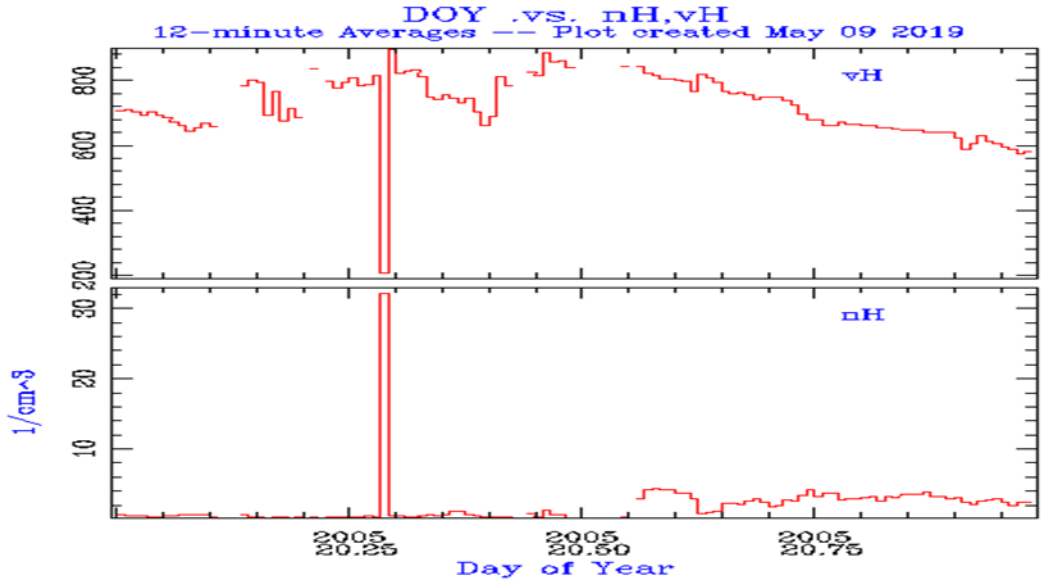

Figure 5. ACE SWICS velocity and density data for 20 January 2005.

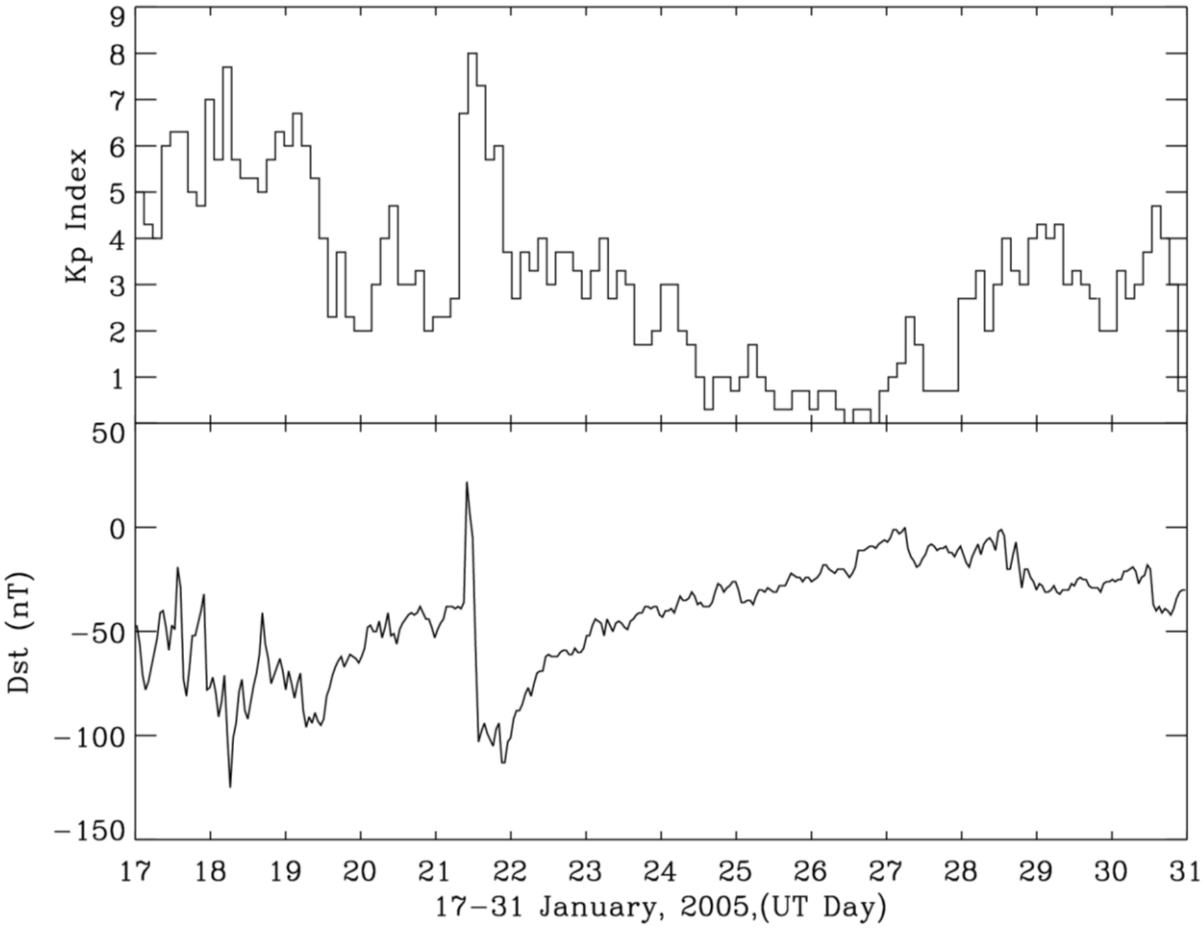

Figure 6. Two magnetic indices during the two week interval containing MINIS flight 2S. Top panel depicts K_p and the bottom panel depicts D_{st}.

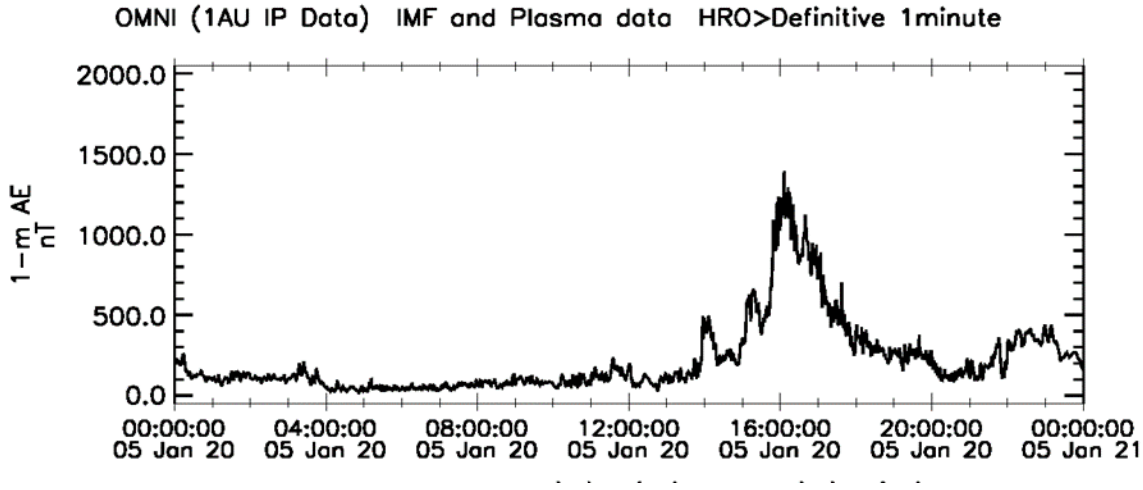

Figure 7. *AE* index on 20 January 2005.

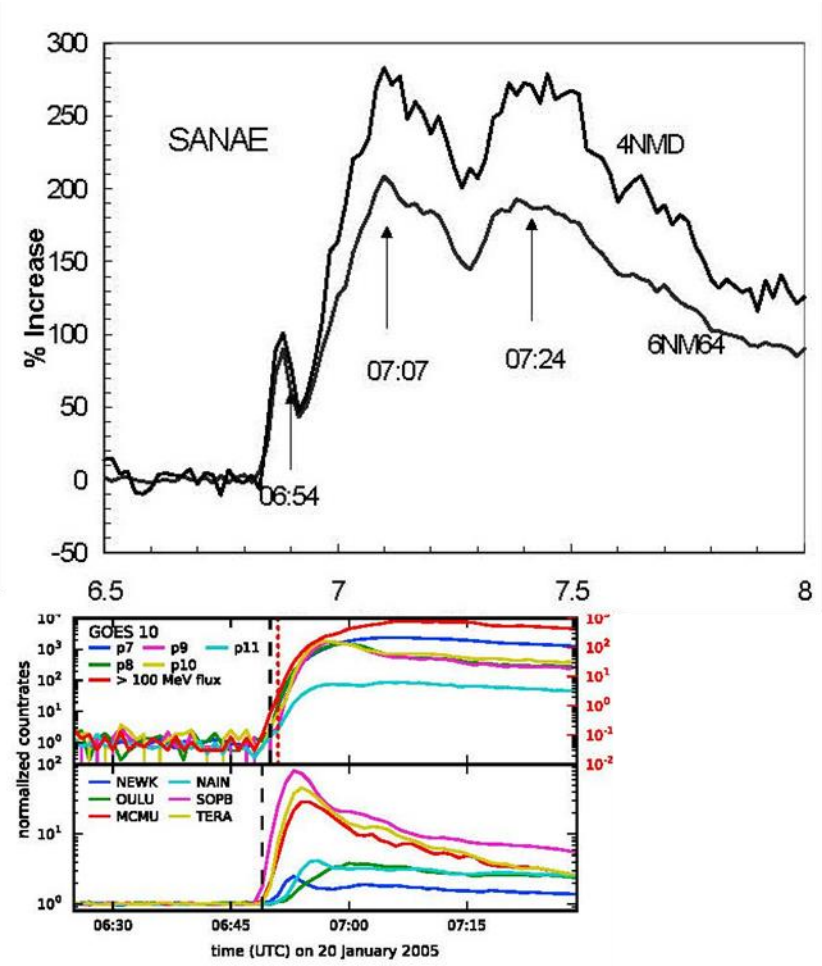

Figure 8. Top panel is top left panel of Figure 1 from *Moraal et al.* [2005], showing the three peaks seen by the SANAE neutron monitor during the GLE of 20 January 2005. Bottom panel is the bottom left panel of Figure 2 in *He and Rodriguez* [2018].Time series of normalized 1 min count rates from neutron monitors (NMs) and GOES 10 EPS and HEPAD channels, as well as 1 min >100 MeV integral fluxes (on the right axes in red). The event onset times detected by each instrument are indicated by a dashed black line, and the event onset times detected in the >100 MeV integral flux data are indicated by a red dotted line. For clarity, only select NMs are shown in the plot.

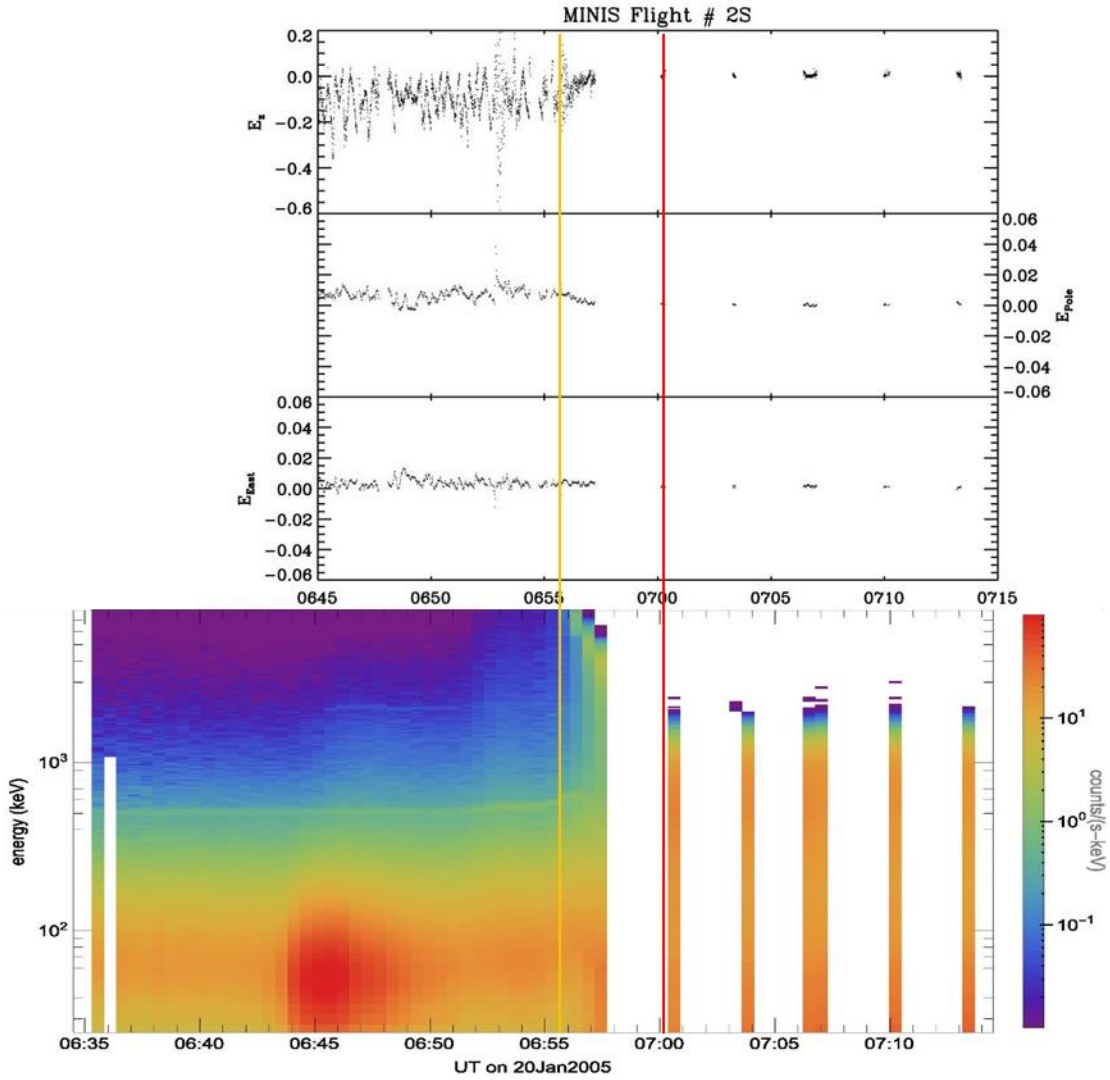

Figure 9. Top three panels present the three components of the electric field in Earth-fixed geomagnetic coordinates. Bottom panel is an energy-time spectrogram from the MINIS X-ray detector for 40 minutes at the time of the X7.1 solar flare on 20 January 2005.

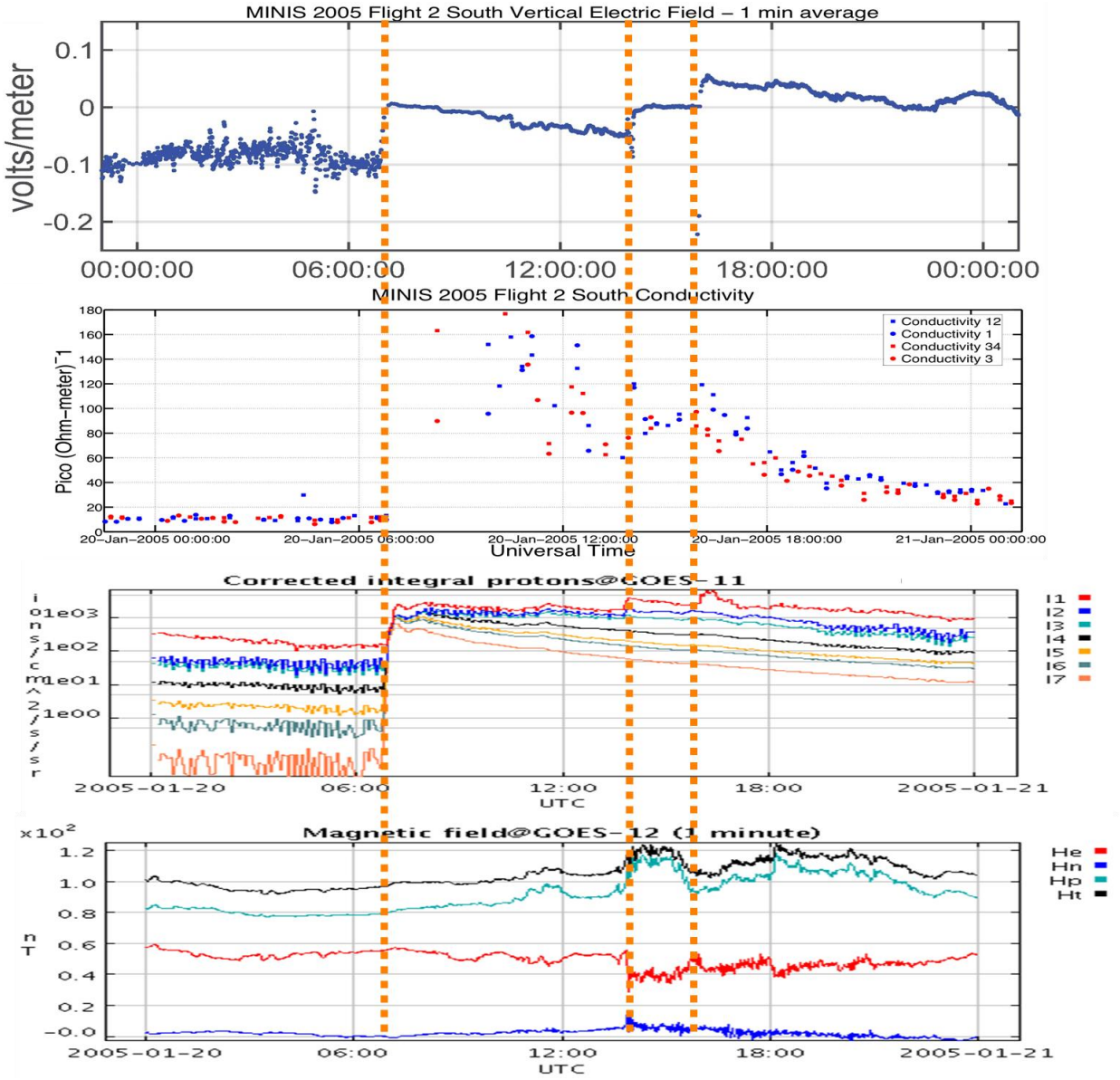

Figure 10. Comparison of GOES and balloon data from the 20 January 2005 flare. Panel (a) at the top of the figure shows 1 min averages of the vertical electric field measured by MINIS Flight 2S for all of 20 January 2005. Panel 10(b), second from top, shows the negative ion conductivity measured by the relaxation technique. Panel 10(c) , third from the top, shows the energetic particle data from GOES 11. Panel 10(d), shows magnetometer data from the GOES 12 geosynchronous spacecraft.

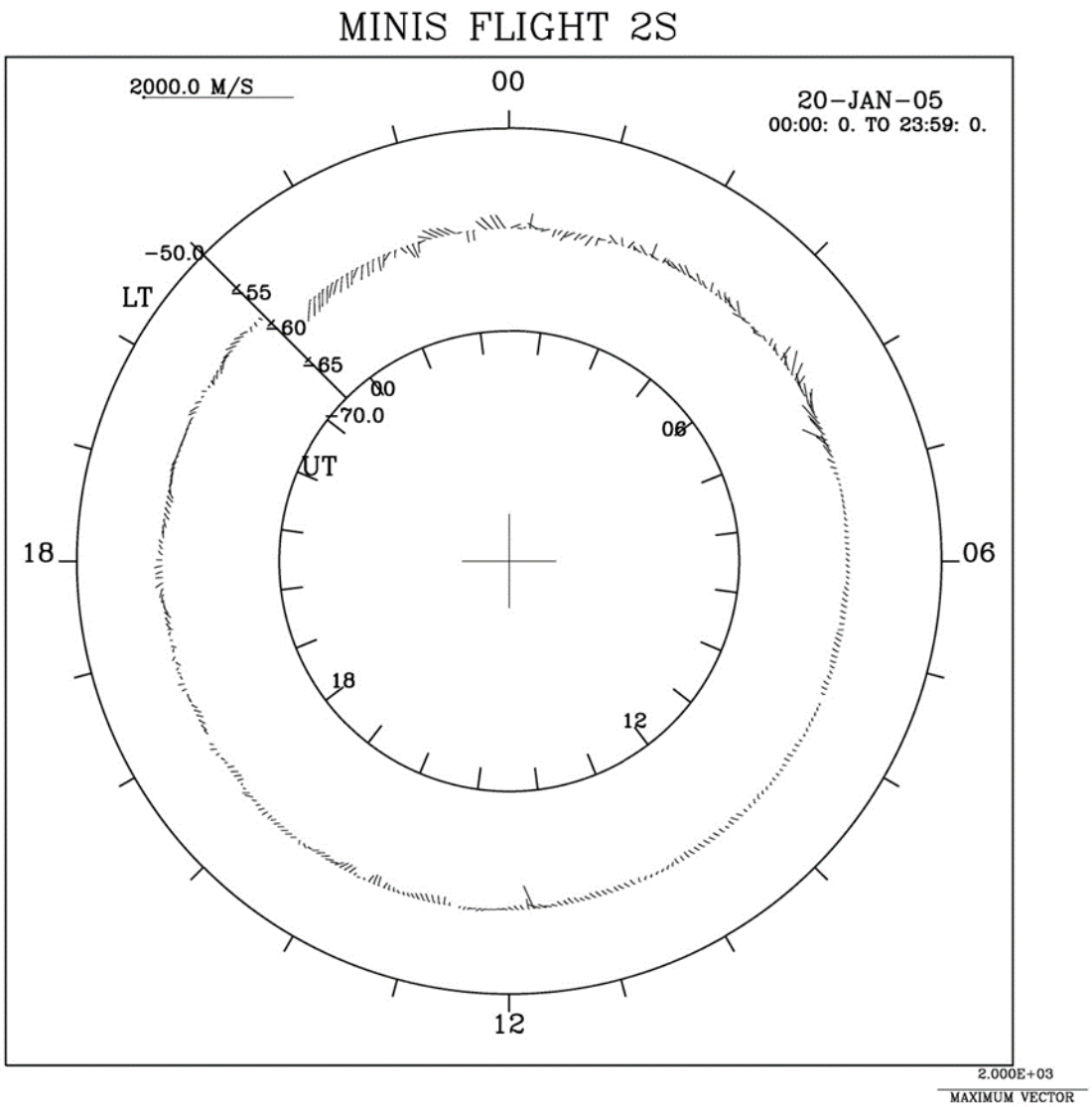

Figure 11 shows the horizontal electric field data plotted as equivalent ionospheric convection in clockdial format. The view is down on the South Pole, which makes the clockface correspond to a normal clock. The outer ring gives the magnetic local time, The inner ring shows the UTC of the observations, with the UTC-MLT conversion fixed at the start of the interval shown. The bar between the rings shows the geomagnetic latitude. The base of each one min average data arrow is at the location of the balloon at the indicated UTC. The arrow represents the ionospheric flow velocity vector.

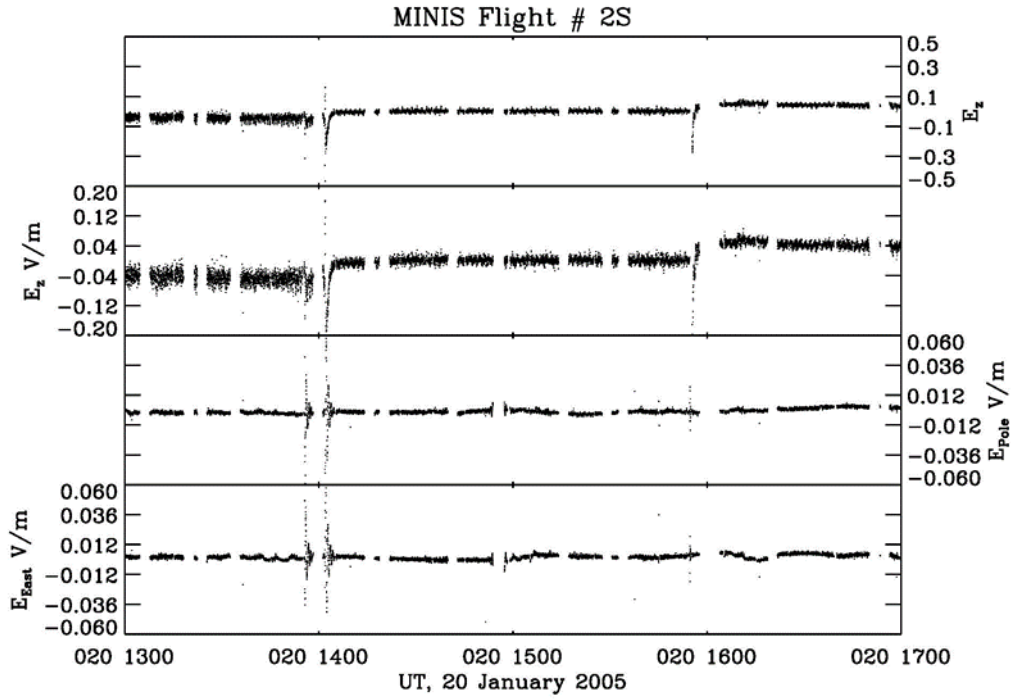

Figure 12. Despun balloon electric field observations plotted in earth-fixed geomagnetic coordinates using a 1 Hz sample rate. From top to bottom, the panels show the vertical field at two gains, poleward, and eastward components. The four-hour interval shown exhibits the 2nd and 3rd step-like changes in the vertical field.

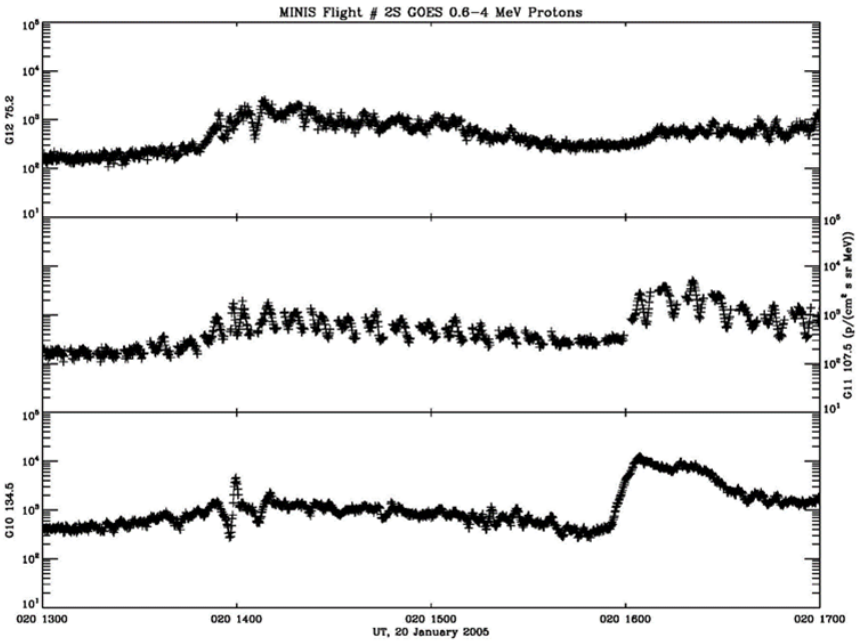

Figure 13. GOES 0.6-4 MeV proton fluxes plotted as a function of UTC for the same interval as Figure 12. Top to bottom, the panels show data from GOES 12, GOES 11, and GOES 10, plotted in East to West order.

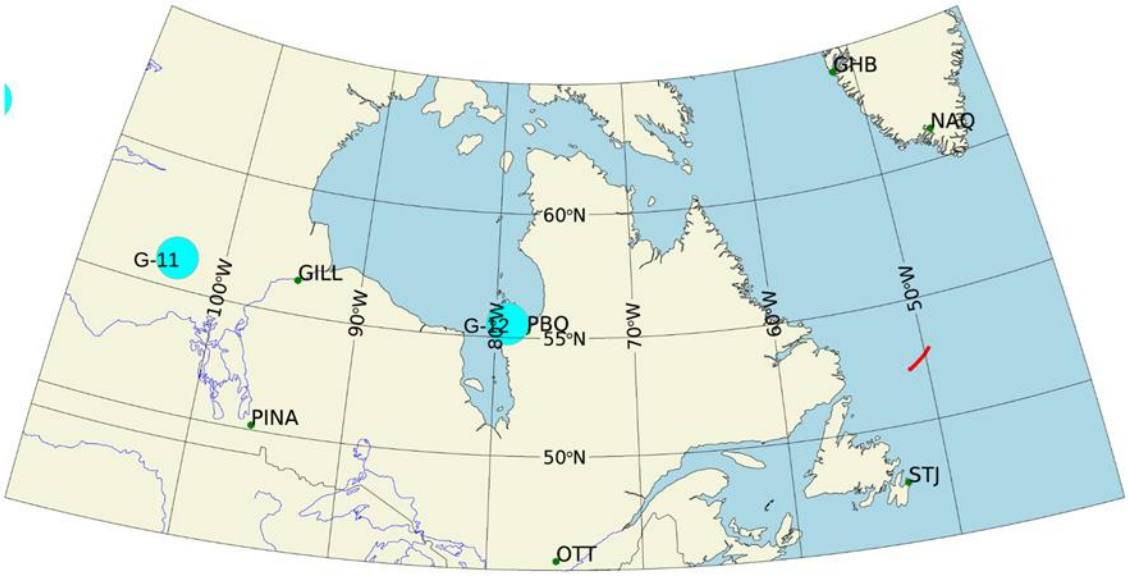

Figure 14. Some data taken in 1650. A map of Canada, showing magnetometer observatories (green dots), GOES conjugate footprints (cyan circles) and balloon conjugate track (red line).

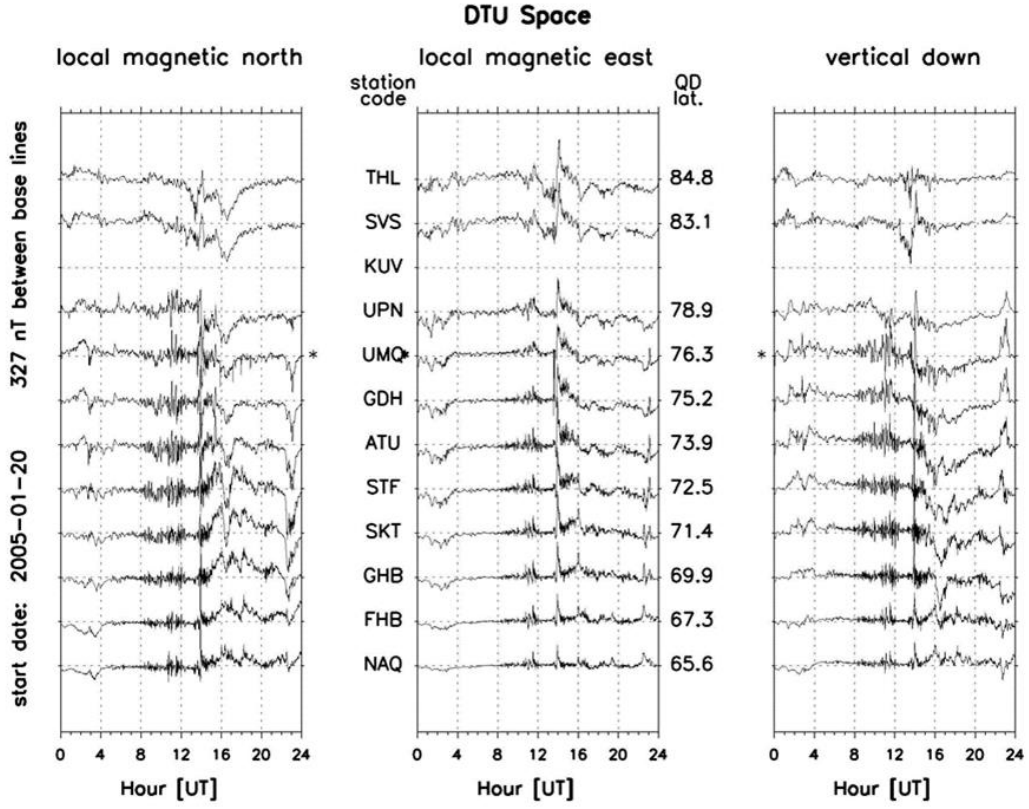

Figure 15. Magnetometer data from the west coast of Greenland during 20 January 2005.

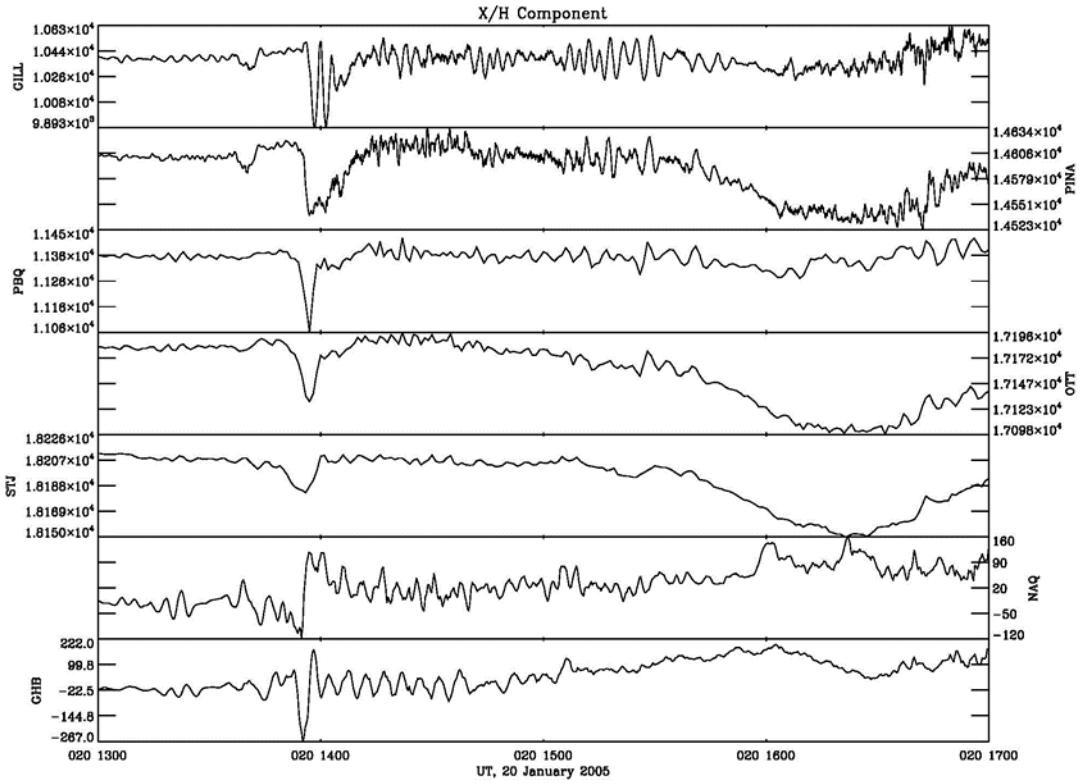

Figure 3. Magnetometer X component from the stations located in Figure 14 plotted vs. UTC for the time interval of Figures 12 and 13.

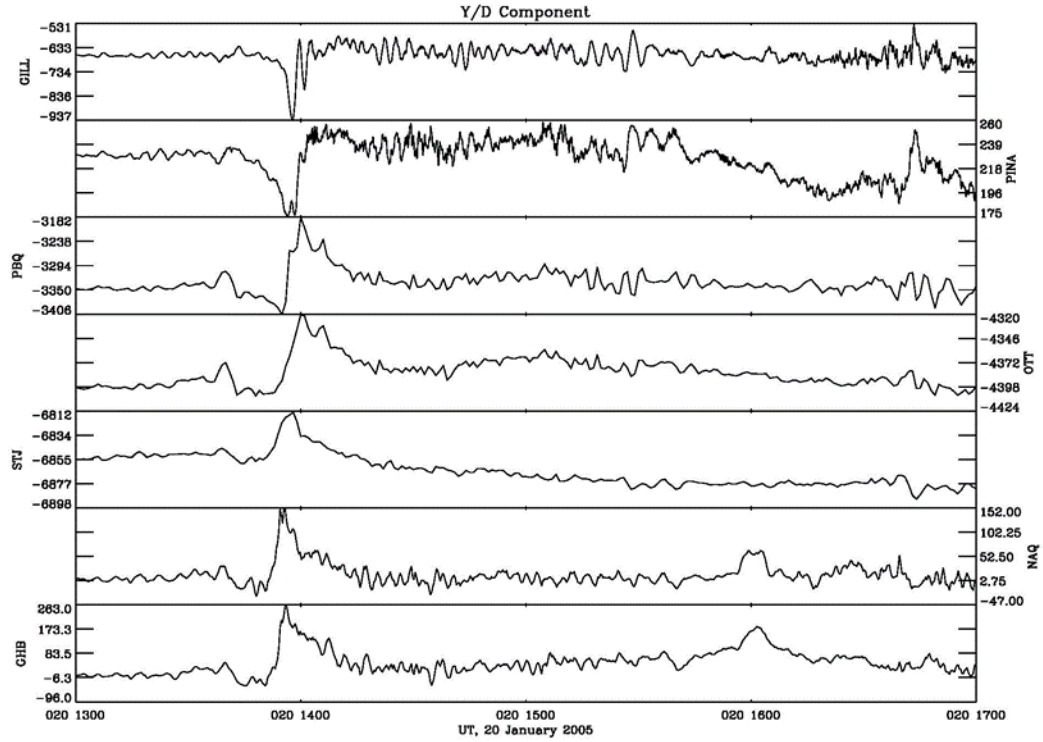

Figure 4. Magnetometer Y component from the same stations and interval as Figure 16.

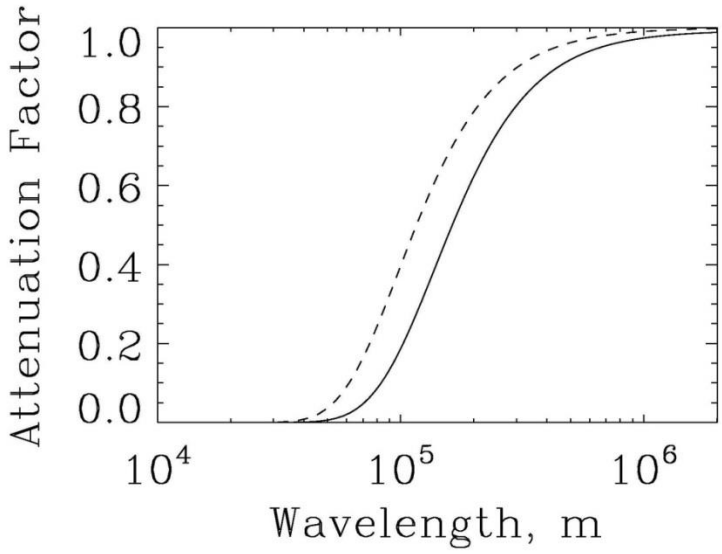

Figure 18. The attenuation factor or transfer function that maps the ionospberic electric field to balloon altitude is plotted as a function of ionospheric electric field wavelength.

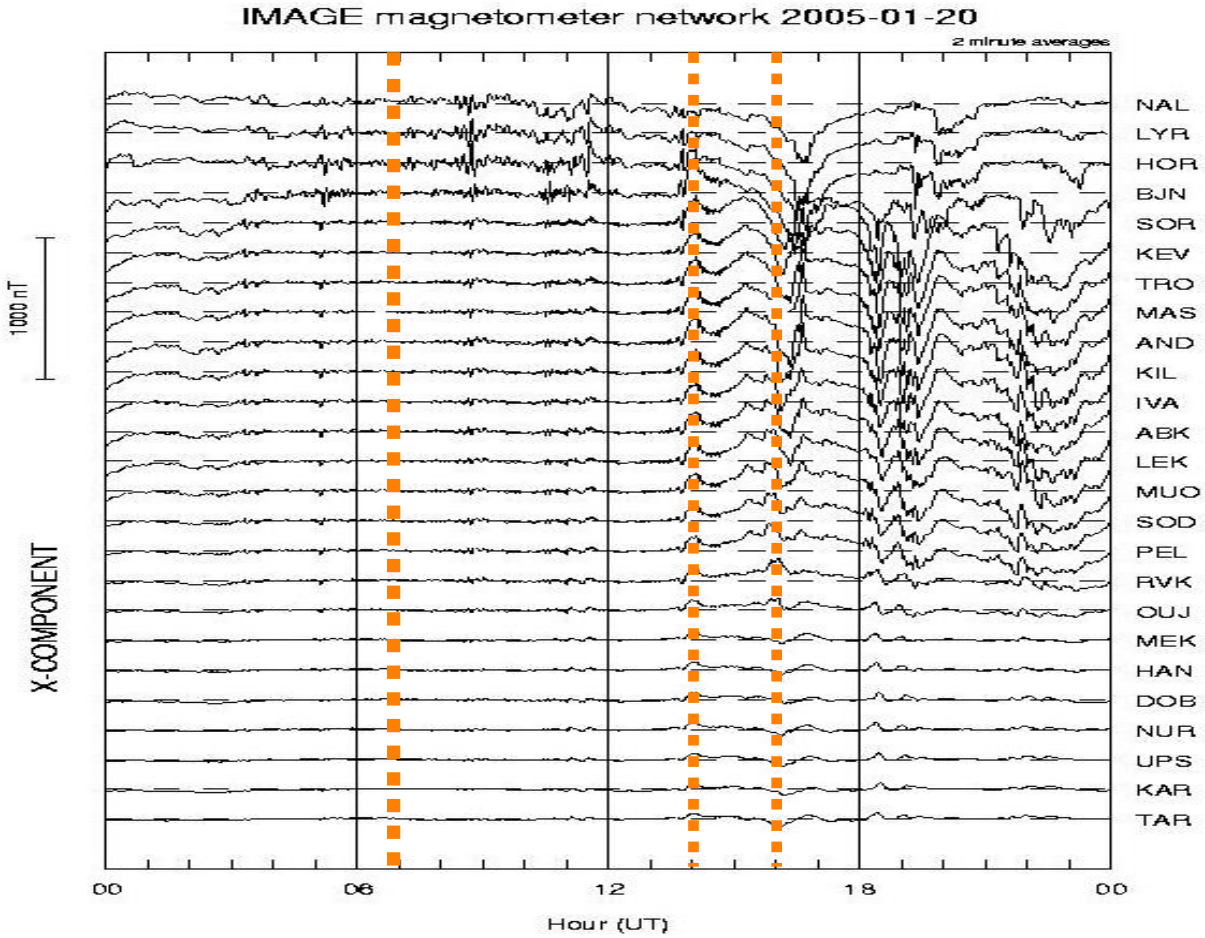

Figure 19. Magnetometer data from the IMAGE network in Scandinavia during 20 January 2005.

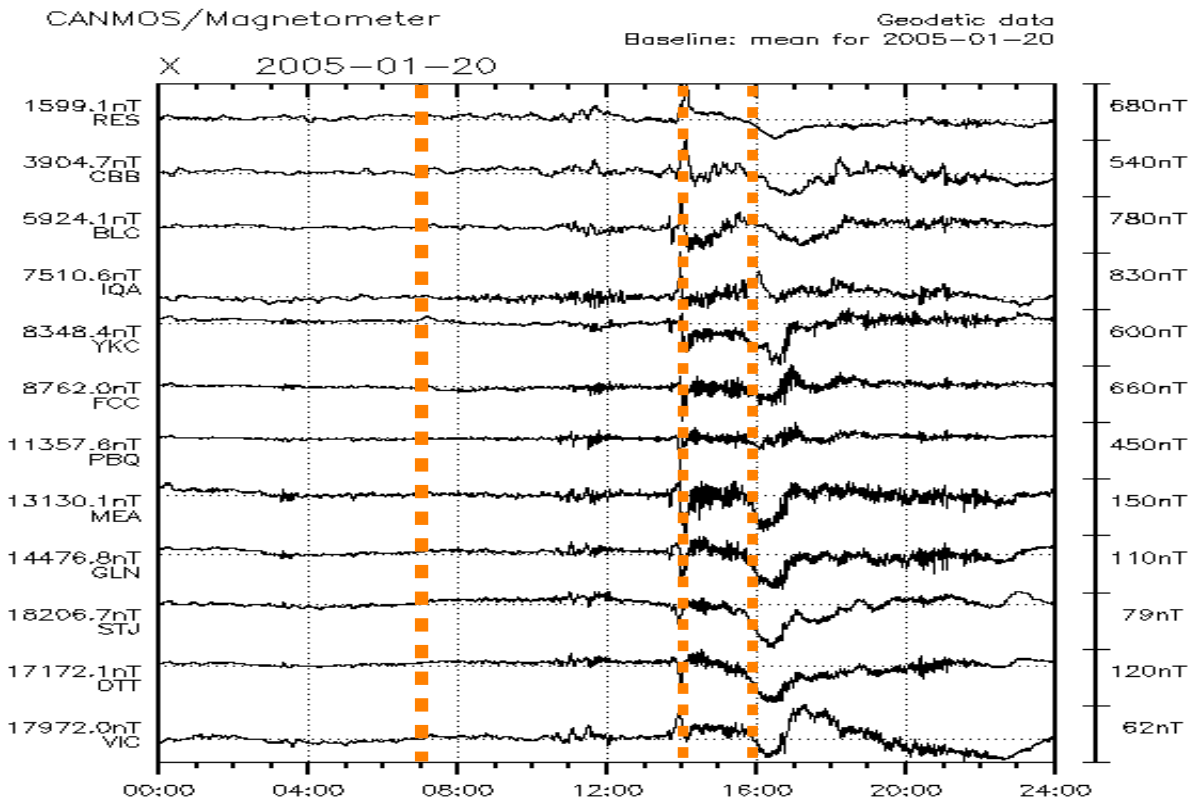

Figure 20. Magnetometer data from the CANMOS network in Canada during 20 January 2005.

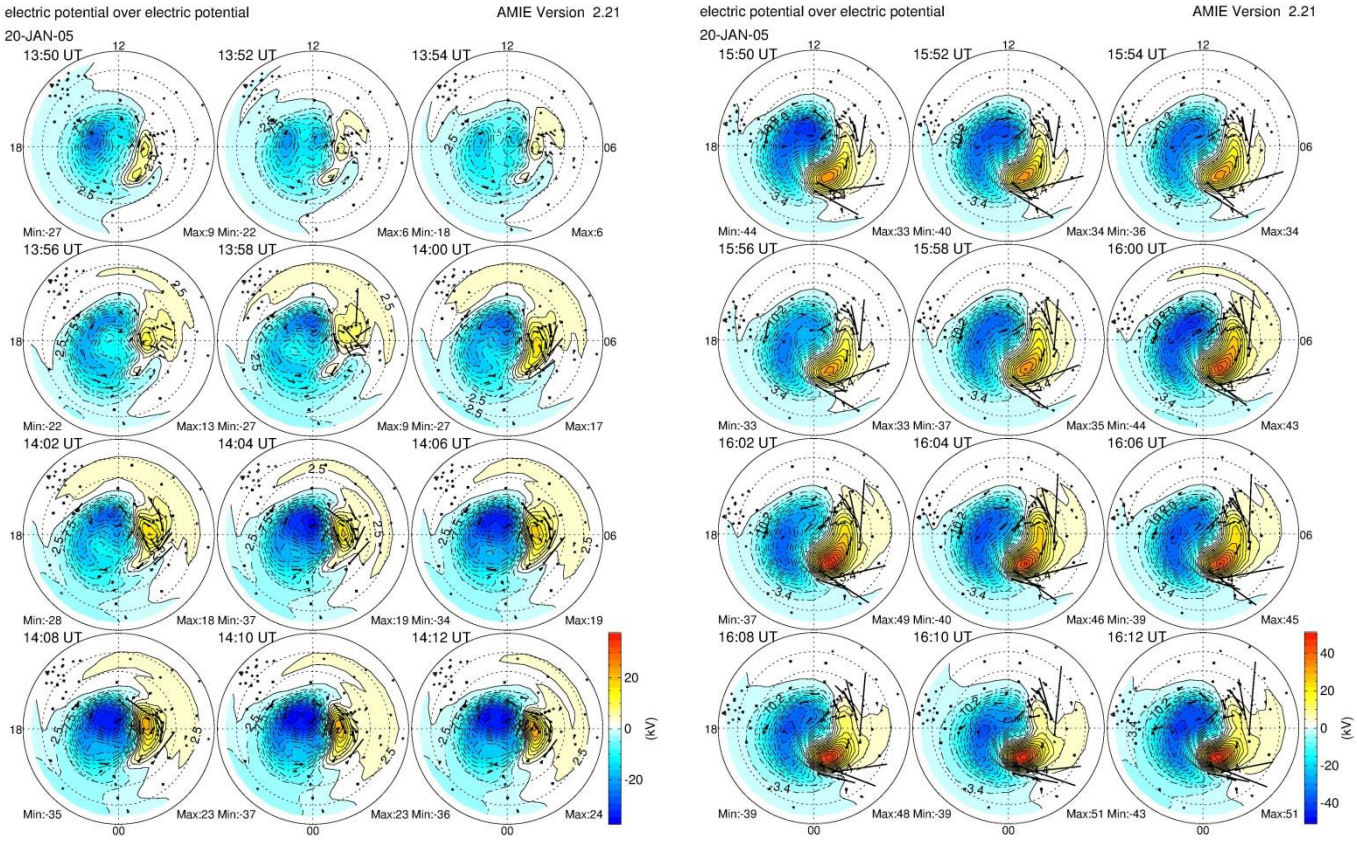

Figure 21 a & b. Models of the Northern Hemisphere ionospheric potential patterns computed by AMIE plotted at 2 minute intervals at the time of the 2nd and 3rd steps.

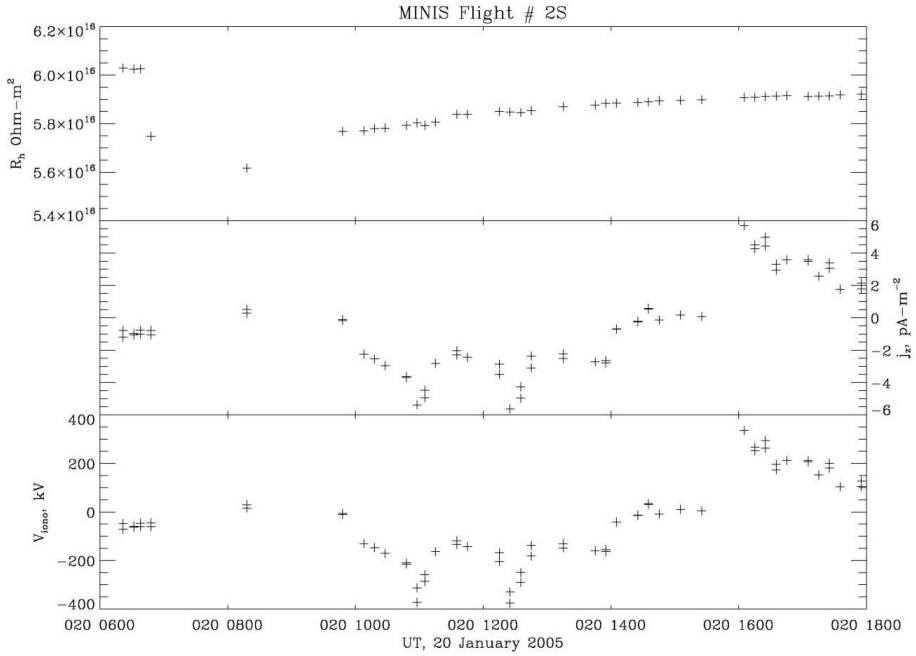

Figure 22. Top to bottom, height integrated column resistance, vertical current density and Earth-ionosphere potential, inferred as described in the text; all plotted as functions of time.

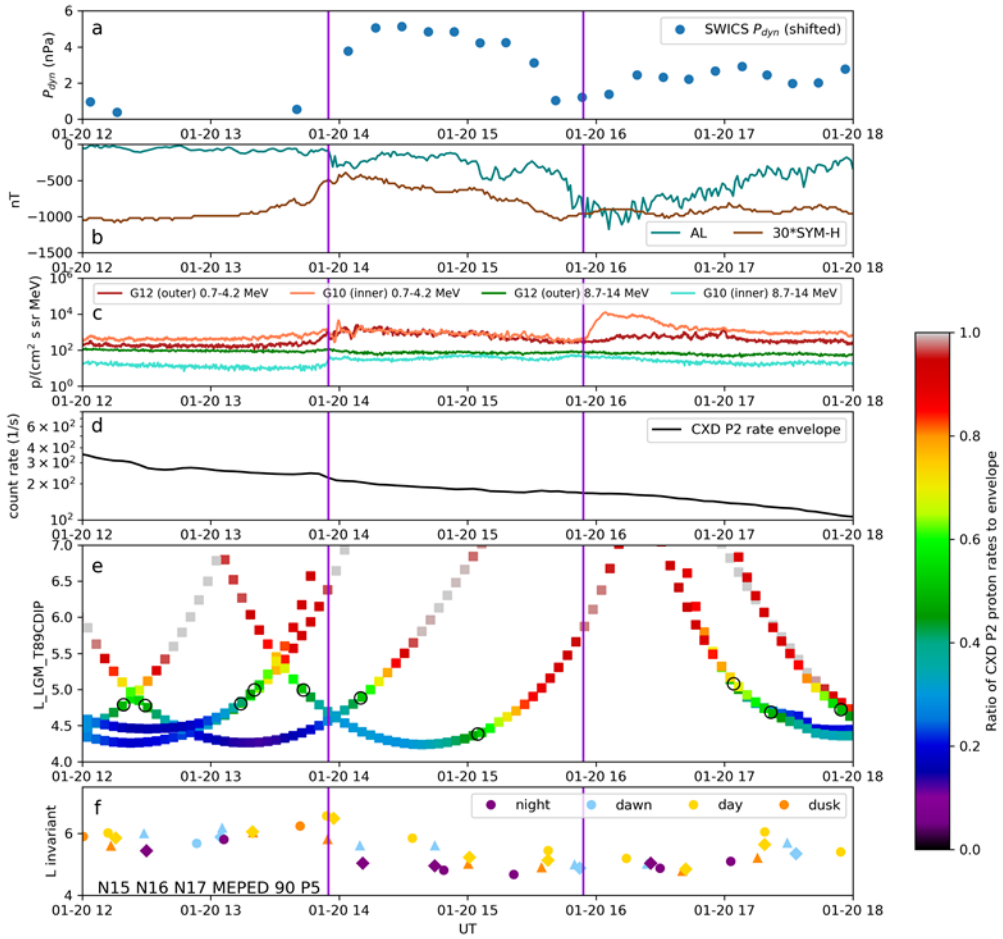

Figure 23. Vertical lines at 1355 and 1554 indicate the times of current bursts observed at MINIS. (a) Solar wind dynamic pressure calculated from ACE SWICS proton and alpha particle density and velocity, shifted by the solar wind travel time to the magnetopause. (b) WDC Kyoto 1-min SYM-H and provisional AL indices. (c) GOES-10 and -12 0.7-4.2 MeV and 8.7-14.5 MeV proton fluxes. (d) Upper envelope of CXD P2 rates (>10 MeV protons) from the five GPS satellites, an estimate of the near-Earth interplanetary solar proton rates level. (e) CXD P2 rates normalized to the upper envelope as a function of time and T89 McIlwain L shell. Open circles indicate cutoff locations, where P2 rates are attenuated to half the interplanetary level. In two cases (c. 1300-1330 and c. 1700-1800), two satellite traces overlap and there are two open circles in close succession, one of which corresponds to the obscured trace. (f) POES MEPED 90-deg telescope P5 cutoffs. Triangles = N15, diamonds = N16, circles = N17.

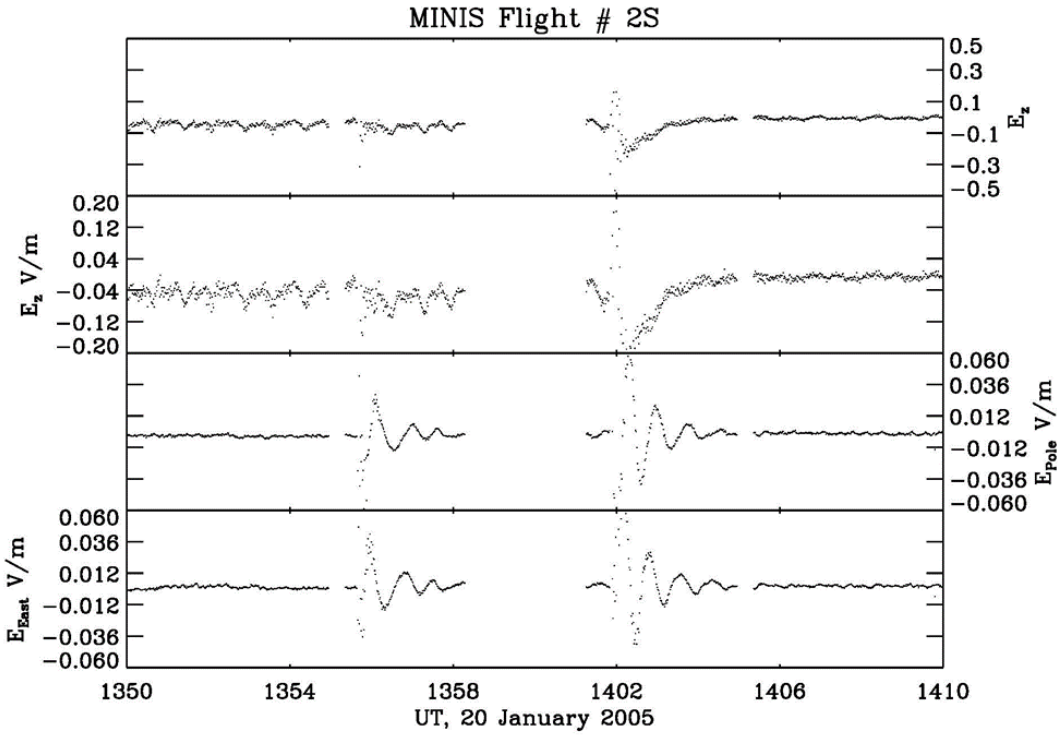

Figure 24. Three components of the electric field in Earth-fixed geomagnetic coordinates plotted at a 1Hz sample rate as a function of UTC. The vertical field is shown at two gains.

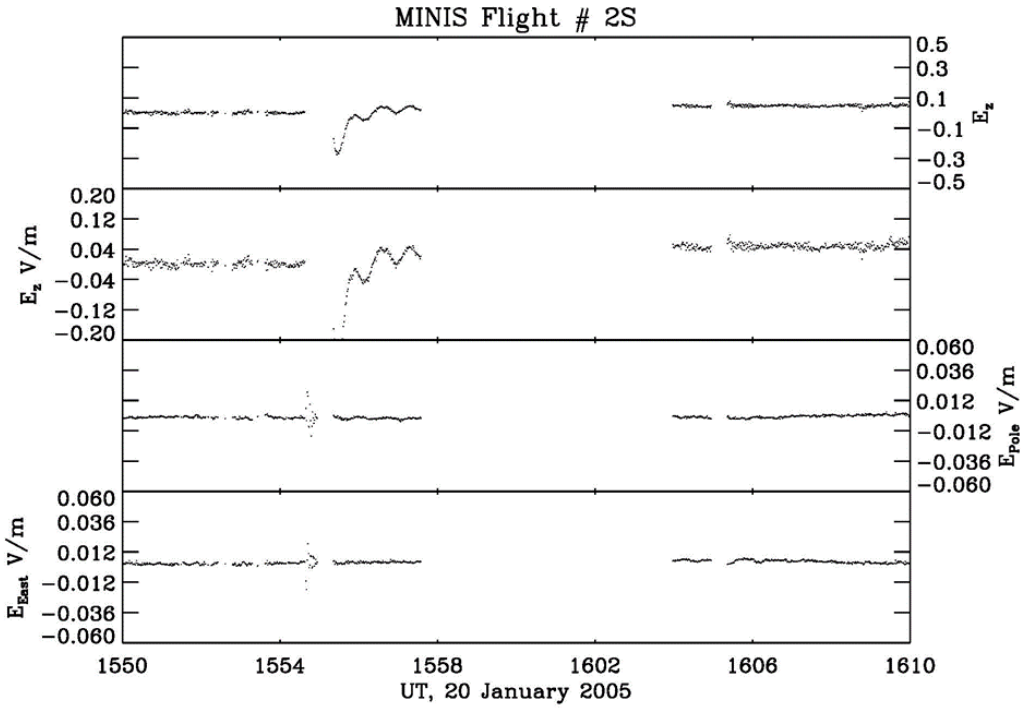

Figure 25. Three components of the electric field in Earth-fixed geomagnetic coordinates plotted at a 1Hz sample rate as a function of UTC. The vertical field is shown at two gains.

Bering, E. A., III (1995), The global circuit: Global thermometer, weather by-product, or climatic modulator?, *Rev. Geophys.*, *33*(U. S. National Report to International Union of Geodesy and Geophysics), 845-862.

Bering, E. A., III, J. R. Benbrook, G. J. Byrne, R. H. Holzworth, and S. P. Gupta (2003), Long term changes in the electrical conductivity of the stratosphere, *Adv. Space Res.*, *32*(9), 1725-1735.

Bering, E. A., III, A. A. Few, and J. R. Benbrook (1998), The global circuit, *Physics Today*, *51*(10), 24-30.

Bering, E. A., III, et al. (2005), Balloon observations of temporal and spatial fluctuations in stratospheric conductivity, *Adv. Space Res.*, *35*, 1434-1449.

Byrne, G. J., J. R. Benbrook, E. A. Bering, III, D. M. Oro, C. O. Seubert, and W. R. Sheldon (1988), Observations of the stratospheric conductivity and its variation at three latitudes, *Journal of Geophysical Research*, *93*, 3879-3892.

Holzworth, R. H., and E. A. Bering, III (1996), Ionospheric electric fields from stratospheric balloon borne probes, in *Space Physics Instrumentation: What Works and What Doesn't*, edited by J. Borovsky and R. Pfaff, American Geophysical Union, Washington, DC.

Israel, H. (1973), *Atmospheric Electricity*, 2nd ed., Natl. Tech. Inform. Serv., U. S. Dept. Commerce, Springfield, Virginia.

Knipp, D. J., et al. (1993), Ionospheric convection response to slow, strong variations in a northward interplanetary magnetic field: A case study for January 14, 1988, *Journal of Geophysical Research: Space Physics*, *98*(A11), 19273-19292, doi:10.1029/93ja01010.

Kokorowski, M., et al. (2008), Magnetospheric electric field variations caused by storm-time shock fronts, *Adv. Space Res.*, *42*, 181-191.

Kokorowski, M., et al. (2006), Rapid fluctuations of stratospheric electric field following a solar energetic particle event, *Geophys. Res. Lett.*, *33*, L20105.

Kokorowski, M., A. Seppälä, J. G. Sample, R. H. Holzworth, M. P. McCarthy, E. A. Bering, and E. Turunen (2012), Atmosphere-ionosphere conductivity enhancements during a hard solar energetic particle event, *Journal of Geophysical Research: Space Physics*, *117*(A5), n/a-n/a, doi:10.1029/2011ja017363.

Markson, R., and D. Kendra (1992), Ionospheric potential measurments at Hawaii and Christmas Island, in *Proceedings 9th International Conference on Atmospheric Electricity*, edited by E. Borisenkov and V. Stepanenko, p. 18, A.I. Voeikov Main Geophysical Observatory, St. Petersburg, Russia.

Millan, R. M. (2011), Understanding relativistic electron losses with BARREL, *J. Atmos. Solar Terr. Phys.*, *73*(11–12), 1425-1434, doi:http://dx.doi.org/10.1016/j.jastp.2011.01.006.

Millan, R. M., R. P. Lin, D. M. Smith, and M. P. McCarthy (2007), Observation of relativistic electron precipitation during a rapid decrease of trapped relativistic electron flux, *Geophys. Res. Lett.*, *34*(10), n/a-n/a, doi:10.1029/2006gl028653.

Millan, R. M., et al. (2005), Global monitoring of relativistic electron precipitation with balloon networks: MINIS and beyond, *EOS, Trans. AGU*, *86*(56), Abstract SM51D-04.

Mozer, F. S., and R. Serlin (1969), Magnetospheric electric field measurements with balloons, *Journal of Geophysical Research*, *74*, 4739.

Reiter, R. (1992), *Phenomena in atmospheric and environmental electricity*, Elsevier Science Publishers B.V., Amsterdam.

Richmond, A. D., et al. (1988), Mapping electrodynamic features of the high-latitude ionosphere from localized observations: Combined incoherent-scatter radar and magnetometer measurements for January 18--19, 1984, *Journal of Geophysical Research*, *93*, 5760.

Ridley, A. J., G. Crowley, and C. Freitas (2000), An empirical model of the ionospheric electric potential, *Geophys. Res. Lett.*, *27*(22), 3675-3678, doi:10.1029/1999gl011161.

Roble, R. G., and I. Tzur (1986), The global atmospheric-electrical circuit, in *The Earth's Electrical Environment*, edited, National Academy Press, Washington, D.C.